
PERGAMON

Journal of Quantitative Spectroscopy & Radiative Transfer 70 (2001) 473–504

Journal of Quantitative Spectroscopy & Radiative Transfer

www.elsevier.com/locate/jqsrt

Radiative properties of cirrus clouds in the infrared (8–13 μm) spectral region

Ping Yang[a,d,*], Bo-Cai Gao[b], Bryan A. Baum[c], Yong X. Hu[c], Warren J. Wiscombe[d], Si-Chee Tsay[d], Dave M. Winker[c], Shaima L. Nasiri[e]

[a] *Scientific Systems and Applications Inc., Lanham, MD, USA*
[b] *Remote Sensing Division, Naval Research Laboratory, Washington, DC, USA*
[c] *NASA Langley Research Center, Hampton, VA, USA*
[d] *Code 913, NASA Goddard Space Flight Center, Greenbelt, MD 20771, USA*
[e] *Cooperative Institute for Meteorological Satellite Studies, University of Wisconsin, Madison, WI, USA*

Abstract

Atmospheric radiation in the infrared (IR) 8–13 μm spectral region contains a wealth of information that is very useful for the retrieval of ice cloud properties from aircraft or space-borne measurements. To provide the scattering and absorption properties of nonspherical ice crystals that are fundamental to the IR retrieval implementation, we use the finite-difference time-domain (FDTD) method to solve for the extinction efficiency, single-scattering albedo, and the asymmetry parameter of the phase function for ice crystals smaller than 40 μm. For particles larger than this size, the improved geometric optics method (IGOM) can be employed to calculate the asymmetry parameter with an acceptable accuracy, provided that we properly account for the inhomogeneity of the refracted wave due to strong absorption inside the ice particle. A combination of the results computed from the two methods provides the asymmetry parameter for the entire practical range of particle sizes between 1 and 10,000 μm over the wavelengths ranging from 8 to 13 μm. For the extinction and absorption efficiency calculations, several methods including the IGOM, Mie solution for equivalent spheres (MSFES), and the anomalous diffraction theory (ADT) can lead to a substantial discontinuity in comparison with the FDTD solutions for particle sizes on the order of 40 μm. To overcome this difficulty, we have developed a novel approach called the stretched scattering potential method (SSPM). For the IR 8–13 μm spectral region, we show that SSPM is a more accurate approximation than ADT, MSFES, and IGOM. The SSPM solution can be further refined numerically. Through a combination of the FDTD and SSPM, the extinction and absorption efficiencies are computed for hexagonal ice crystals with sizes ranging from 1 to 10,000 μm at 12 wavelengths between 8 and 13 μm.

Calculations of the cirrus bulk scattering and absorption properties are performed for 30 size distributions obtained from various field campaigns for midlatitude and tropical cirrus cloud systems. Ice

*Corresponding author. Code 913, NASA/Goddard Space Flight Center, Greenbelt, MD 20771, USA. Tel.: +1-301-614-6127; fax: +1-301-614-6307.

E-mail address: pyang@climate.gsfc.nasa.gov (P. Yang).

0022-4073/01/$ - see front matter
PII: S0022-4073(01)00024-3

crystals are assumed to be hexagonal columns randomly oriented in space. The bulk scattering properties are parameterized through the use of second-order polynomial functions for the extinction efficiency and the single-scattering albedo and a power-law expression for the asymmetry parameter. We note that the volume-normalized extinction coefficient can be separated into two parts: one is inversely proportional to effective size and is independent of wavelength, and the other is the wavelength-dependent effective extinction efficiency. Unlike conventional parameterization efforts, the present parameterization scheme is more accurate because only the latter part of the volume-normalized extinction coefficient is approximated in terms of an analytical expression. After averaging over size distribution, the single-scattering albedo is shown to decrease with an increase in effective size for wavelengths shorter than 10.0 μm whereas the opposite behavior is observed for longer wavelengths. The variation of the asymmetry parameter as a function of effective size is substantial when the effective size is smaller than 50 μm. For effective sizes larger than 100 μm, the asymmetry parameter approaches its asymptotic value. The results derived in this study can be useful to remote sensing studies of ice clouds involving IR window bands.

Keywords: Cirrus; Crystal; Infrared

1. Introduction

Cirrus clouds form a unique component of the atmosphere and significantly regulate the Earth's radiation energy budget [1–3] because of their large spatial coverage and temporal persistence. And yet, the radiative forcing of these clouds is far from being well understood because of the wide range of observed cirrus cloud properties such as height, optical thickness, particle size, and habit. With the recognition of the importance of cirrus clouds, a number of programs have been established to investigate global cirrus properties. For instance, intensive field observations regarding cirrus clouds have been conducted as a major component of the First ISCCP Regional Experiment (FIRE) (Phase-I in October 1986 and Phase-II in November–December 1991) [4], the European experiments on cirrus (ICE/EUCREX) carried out in 1989 [5]. Additional cirrus field campaigns are being planned, such as the Cirrus Regional Study of Tropical Anvils and Cirrus Layers (CRYSTAL). Besides these field campaigns, new instrumentation has been developed for use in space- or aircraft-borne measurement programs. Such programs include the Lidar In-space Technology Experiment (LITE) [6], the MODerate resolution Imaging Spectrometer (MODIS) [7], and the future Pathfinder Instruments for Cloud and Aerosol Spaceborne Observations-Climatologie Etendue des Nuages et des Aerosols (PICASSO-CENA) [8]. The data obtained from these instruments will enhance our capability to detect cirrus clouds and to retrieve their microphysical and optical properties on a global scale with a substantial temporal span.

A number of studies have proposed methods to infer global cirrus properties from infrared (IR) radiance measurements. One benefit to using IR methods to infer cloud properties rather than those that incorporate visible or near-infrared bands is that cloud properties are more consistent between daytime and nighttime conditions. The IR techniques are also independent of the sun glint associated with the specular reflection over water which is prevalent in daytime data. The IR CO_2 slicing technique is effective in inferring cirrus height and effective

cloud amount (emittance multiplied by cloud fraction) [9,10]. Various IR algorithms to infer cirrus particle size have been suggested (see e.g., Refs. [11,12]), whereas the methods to infer cloud thermodynamic phase using data from the 8.52, 11, and 12 μm bands have been demonstrated by Strabala et al. [13] and Baum et al. [14]. There have been advances in recent years in the development and use of well-calibrated aircraft-based interferometers, such as the High Spectral Resolution Infrared Spectrometer (HIS) [15–17] and the National Polar Orbiting Operational Environmental Satellite System (NPOESS) Aircraft sounding Testbed-Interferometer (NAST-I) [18]. In coming years, the spectral resolution of IR data measured from space will increase greatly when interferometers are launched, such as Infrared Atmospheric Sounder Interferometer (IASI) on EUMETSAT, the Geostationary Imaging Fourier Transform Spectrometer (GIFTS), and the NPOESS Crosstrack Infrared Sounder (CRIS). With an interferometer, cloud measurements may be recorded at thousands of wavenumbers simultaneously. To date, however, few studies have explored the use of infrared interferometer data for cirrus cloud property retrieval. The remote sensing of cirrus cloud properties from IR interferometer data has been hampered by the difficulty in determining accurately the fundamental bulk scattering properties for a realistic range of crystal sizes and shapes at IR wavelengths where the applicability of the ray-tracing method breaks down [19].

Cirrus clouds are composed of almost exclusively nonspherical ice crystals, as is evident from the observations based on aircraft-borne two-dimensional optical cloud probes (2D-C) and balloon-borne replicator images (e.g., Refs. [20,21]). It has been shown that the spherical approximation for nonspherical ice crystals in terms of equivalent volume or projected-area is inadequate and often misleading, as is illustrated by Liou et al. [22]. In practice, an incorrect specification of the ice crystal model in retrieving the optical thickness of cirrus clouds from satellite-borne measurements can lead to an underestimation or overestimation of the actual optical thickness by a factor that can exceed 3 [23]. Thus nonsphericity of ice crystals must be accounted for in the development of a reliable retrieval algorithm. On this specific issue, the significance of using reliable single-scattering properties of ice crystals to generate look-up tables for retrieval implementation and the parameterization of the bulk radiative properties of cirrus clouds has been demonstrated and articulated in a number of recent publications (e.g., Refs. [14,24–33]). Although substantial progress has been made in the study of scattering and absorption by ice crystals [24,34], there is not a single method that can cover the entire size parameter spectrum for light scattering computations. To derive the scattering and absorption properties of nonspherical ice crystals, Liou et al. [22] developed the concept of a unified theory. This unified theory is based on a combination of a numerically accurate finite-difference time-domain technique (FDTD) [35–40] for small particles and an improved geometric optics method (IGOM) [41,42] for large particles at visible and near-infrared wavelengths. However, for IR wavelengths where strong absorption is involved, there is a discontinuity between the FDTD and IGOM results at size parameters on the order of 20, which is in practice the computational limit for the FDTD method given current computer resources. One cause of this discontinuity is the tunneling or the above-edge effect [43]. Several approximate methods [29,30,44,45] suggested to account for the tunneling effect are based on parameterizations involving Mie theory, a combination of Mie theory and the geometric optics method, or the complex angular momentum theory developed by Nussenzveig and Wiscombe [46,47].

The intent of this study is to develop methodology capable of deriving the fundamental scattering and absorption properties of nonspherical ice crystals, specifically hexagonal columns, that span a size range of 1 to 10,000 μm, over a wavelength range from 8 to 13 μm. Absorption effects in ice crystals can be appreciable in this IR wavelength range. In Section 2, we present methodology for calculating the scattering properties at infrared wavelengths. In particular, we present the stretched scattering potential method (SSPM) to calculate the extinction and absorption cross sections. In Section 3, we present the bulk radiative properties and parameterization for cirrus clouds. Finally, the conclusions of this study are given in Section 4.

2. Computation of optical properties for ice crystals at infrared wavelengths

2.1. Aspect ratio for ice crystals and selection of wavelengths

A variety of nonspherical ice crystal habits, or shapes, have been observed in cirrus clouds, including hexagonal columns and plates, bullet rosettes, and complex aggregates. To demonstrate our methodology, in this study we simplify the complexity of determining what best represents the habit distribution in cirrus by assuming cirrus are composed solely of hexagonal columns with random orientations in space. It should be pointed out that the scattering properties for columns and plates can be substantially different; in particular, it has been shown that the tunneling contributions for hexagonal plates are much smaller than for columns [48]. Although the percentage of pristine ice clouds in cirrus clouds are normally low [49], studies of in situ cirrus measurements have demonstrated that the upper layers of midlatitude cirrus cloud systems are often comprised of pristine hexagonal crystals [50]. Hexagonal ice crystals are capable of producing 22° and 46° halos and other optical phenomena by scattering incident solar radiation at short wavelengths. The hexagonal shape model has been assumed often in previous studies concerning cirrus clouds [24–30,51–53]. Upwelling radiances in the infrared wavelengths tend to be dominated by thermal emission from the uppermost portions of the cloud because the contributions from lower cloud portions are largely absorbed, provided the cloud is not very thin.

To carry out scattering calculations, we define the aspect ratio for ice crystals at various sizes as follows:

$$2a/L = \begin{cases} 1, & L \leqslant 40\ \mu\text{m}, \\ \exp[-0.017835(L-40)], & 40 < L \leqslant 50\ \mu\text{m}, \\ 5.916/L^{1/2}, & L > 50\ \mu\text{m}, \end{cases} \tag{1}$$

where a is the semi-width of cross section and L is the length of an ice crystal. The aspect ratio defined by Eq. (1) roughly corresponds to the observations reported by Ono [54] and Auer and Veal [55]. Fig. 1 shows a comparison of the aspect ratio defined in this study with that of Takano and Liou [51], who used only five size-bins in discretizing the size distribution for ice crystals. Excellent agreement is evident for the comparison. In the D–L plot of Fig. 1 in which $D = 2a$ is the width of cross section, the continuous D–L is not smooth at a size of $L = 40$ μm because of an abrupt variation in the derivative of aspect ratio. However, this effect is very small.

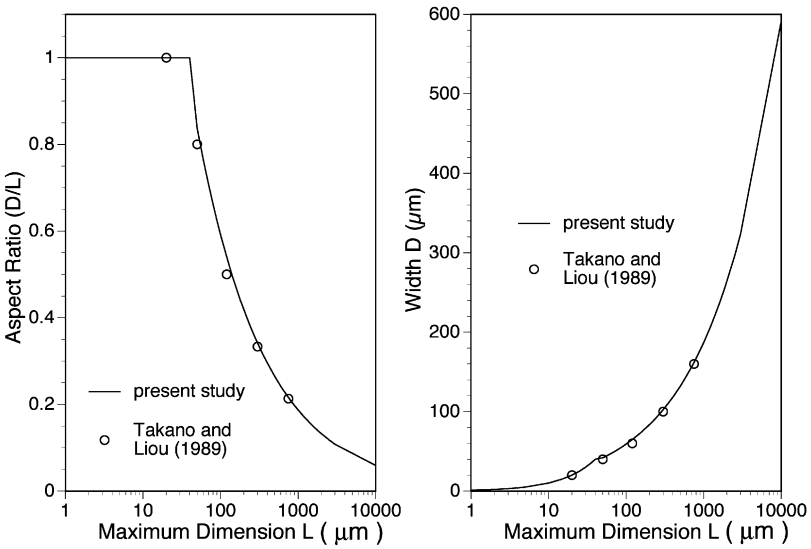

Fig. 1. The aspect ratio used for defining the geometry of the hexagonal ice crystals. D and L are the width of cross section and length of the particle, respectively. Results from this study are compared to those of Takano and Liou [51].

To economize the computational effort, the scattering calculations are performed for 12 wavelengths between 8 and 13 μm, which are selected at 8.0, 8.5, 9.0, 9.5, 10.0, 10.5, 10.8, 11.0, 11.5, 12.0, 12.5, and 13.0 μm. The choice of these wavelengths is based on the characteristics of ice refractive index compiled by Warren [56], as is shown in Fig. 2. The dotted vertical lines indicate the locations of the selected wavelengths. Note that the variation of the refractive index is essentially linear in the intervals of the selected wavelengths. Because of the quasi-linear variation of the refractive index versus wavelength in a given small spectral interval, the scattering and absorption properties at any arbitrary wavelength in the 8–13 μm region can be approximated by an interpolation of those calculated at the selected wavelengths. We also note that near 10.8 μm there exists a region of extremely strong absorption, often called by Christiansen band [57,58]. Near 10.8 μm, the real part of the refractive index has a value close to 1 and the extinction efficiency reaches a minimum. As is evident from Fig. 2, the imaginary part of the refractive index is significant at the Christiansen band, leading to the dominance of the absorption effect in the extinction process. The behavior of ice absorption in the Christiansen band has been shown in laboratory measurements [58,59] and a theoretical explanation was reported by Yang et al. [60].

2.2. Asymmetry parameter for angular distribution of scattered energy

The angular distribution of the energy scattered by a particle is defined by its scattering phase function. At IR wavelengths, the phase function of an ice crystal is essentially featureless when compared to that at a visible or near-infrared wavelength. The primary scattering features

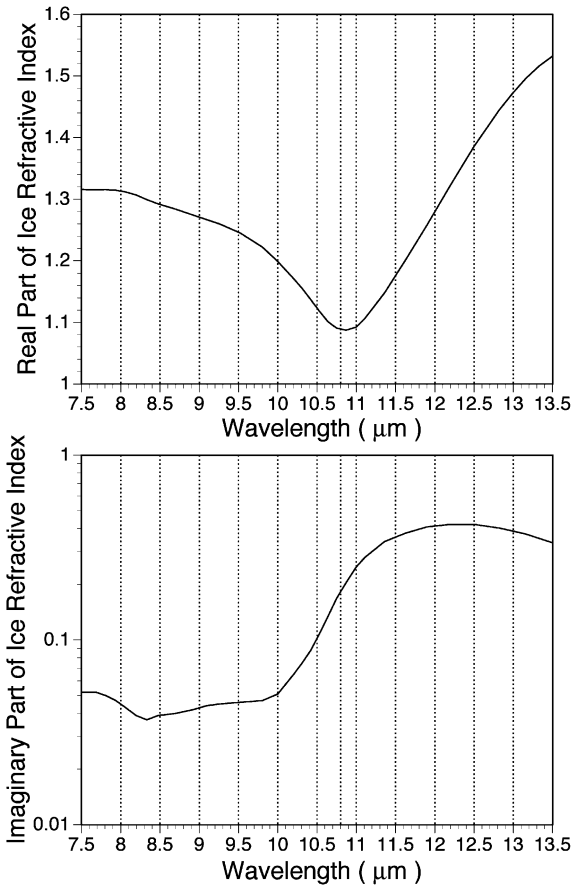

Fig. 2. The variation of refractive index in IR (7.5–13.5 μm) region. The refractive index data are those compiled by Warren [56]. The dotted lines in the diagrams indicate the locations of the wavelengths selected for the presented scattering computation.

of a hexagonal crystal at a visible wavelength, such as the halo peaks and backscattering enhancement, are smoothed out at IR wavelengths because of absorption.

For radiative transfer calculations at IR wavelengths, the detailed information of the phase function is unnecessary because the multiple scattering effect is only on the order of a few percent. Thus, the asymmetry parameter that describes the magnitude of the deviation of particle phase function from isotopic scattering is very useful at IR wavelengths, which is defined as follows:

$$g = \frac{1}{2} \int_0^{\pi} P(\theta) \cos\theta \sin\theta \, \mathrm{d}\theta, \tag{2}$$

where $P(\theta)$ is the normalized phase function. Given the asymmetry factor associated with an IR phase function of nonspherical ice crystals, an accurate phase function for a given size

distribution of ice crystals can be approximated by the well-known Henyey–Greenstein analytical function

$$P_{\mathrm{HG}}(\theta) = \frac{1-g^2}{(1+g^2-2g\cos\theta)^{3/2}} = \sum_{l=0}^{N}(2l+1)g^l P_l(\cos\theta), \tag{3}$$

where $P_l(\cos\theta)$ is the set of Legendre polynomials employed for the decomposition of the phase function. The advantage of using the Henyey–Greenstein phase function in radiative transfer calculations lies in its simplicity and efficiency in the expansion of a phase function in terms of Legendre function. There is a physical justification for such a simplification. For an IR wavelength, the phase function calculated for a given size distribution of ice crystals tends to be smooth at sidescattering and backscattering angles whereas a strong diffraction peak is typically noted in the forward scattering direction. The forward peak may need to be truncated; for this the delta-M method developed by Wiscombe [61] may be employed. The truncated phase function can be well approximated by the analytical Henyey–Greenstein function at the IR wavelengths relevant to our study.

The FDTD technique is employed to solve for the scattering and absorption properties for ice crystals whose maximum dimensions are smaller than 40 μm. The FDTD method solves the interaction of electromagnetic waves with a particle of any given shape and is based on the finite-difference analog of the time-dependent Maxwell equations. The strength of this method is its simplicity in concept, computational flexibility, and robust nature in dealing with light scattering problems involving nonspherical and/or inhomogeneous particles. The disadvantage of this method is its tremendous demand on computational resources when the size parameter is larger than 20. Detailed descriptions of the FDTD method may be found in Yang and Liou [38].

To calculate the asymmetry parameter for ice crystals larger than 40 μm, we use a hybrid method based on the improved geometric optics principle (IGOM) and the electromagnetic integral equations [41,42]. At IR wavelengths, the refractive wave inside an ice crystal is inhomogeneous because the planes of constant phase are not parallel to the planes of constant amplitude [62]. This inhomogeneity affects both the ray direction and the reflection/refraction components at the air–particle interface [35]. In particular, the Fresnel coefficients are not unique when absorption is involved, as was shown recently by Yang et al. [63], who further determined the proper form of the reflection/refraction coefficients that should be used in ray-tracing calculations. We have accounted for this improvement in the present set of scattering calculations.

Fig. 3 shows the asymmetry parameter calculated by the FDTD and the IGOM over a range of ice crystal sizes at wavelengths 8.5, 11, and 12 μm. The radiative information at these three wavelengths are being used to retrieve cloud thermodynamic phase in MODIS data. For comparison of results between spherical and nonspherical particles, results computed from Mie theory for equivalent ice spheres are provided in Fig. 3. Following work by Francis et al. [5], Mitchell and Arnott [64], Fu et al. [29], Yang et al. [65], and Grenfell and Warren [66], we

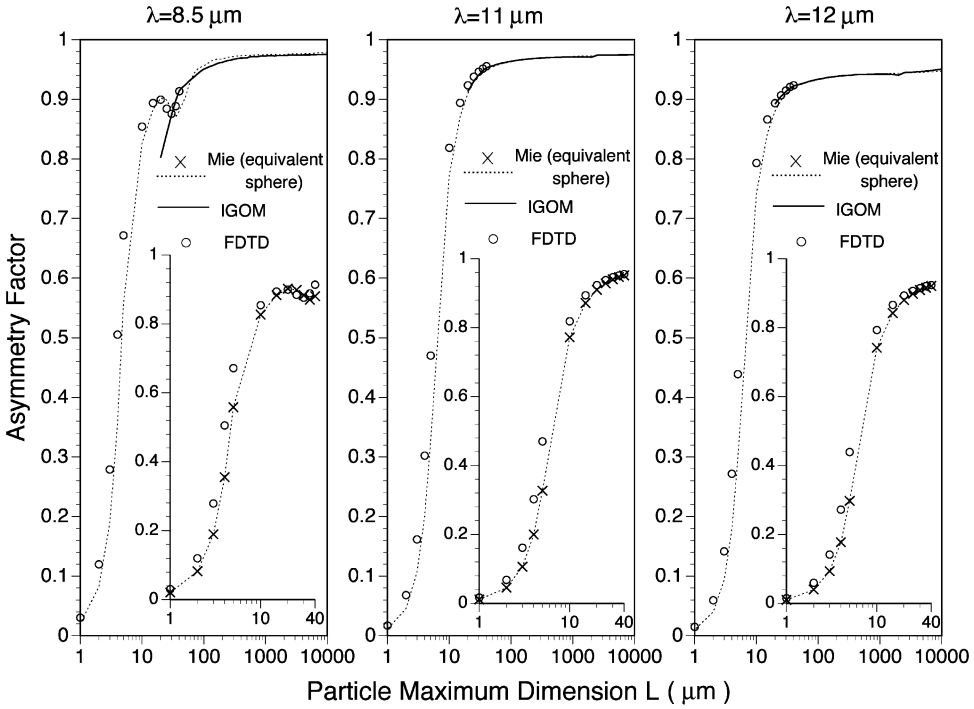

Fig. 3. The asymmetry parameter computed from the FDTD technique and the improved geometric optics method (IGOM) for hexagonal ice crystals at three wavelengths. The subdiagrams are the enlargements for particle sizes between 1 to 40 μm. The Mie solutions are for the equivalent spheres whose radii are defined by Eq. (4). For clarity, the discrete Mie results are not indicated by symbol × in the full-scale diagrams.

define the radius of the equivalent sphere for an individual hexagonal ice crystal as follows:

$$r_e = \frac{3}{4}\left(\frac{\text{volume}}{\text{projected-area}}\right) = \frac{3}{4}\left(\frac{\sqrt{3}a^2L}{\sqrt{3}a^2/2 + aL}\right), \tag{4}$$

where a and L are the semi-width and the length of ice crystal, respectively. The advantage of the preceding definition over those for equivalent volume (or projected-area) is that both volume and area are conserved in approximating the nonspherical particle in terms of a polydisphere system of the equivalent spheres. The inserted subdiagrams in Fig. 3 provide enlargements for ice crystal sizes of 1–40 μm. For small ice crystals with sizes of 3–9 μm, the asymmetry parameters computed from Mie theory for the equivalent spheres and the FDTD technique for the nonspherical particles are quite different. For sizes larger than 100 μm, the IGOM results essentially converge to the Mie results. This convergence occurs because the rays refracted into the particles are almost entirely absorbed and the diffraction and external reflection contributions dominate the scattered energy. Under random orientation conditions, diffraction and external reflection are not sensitive to the details of particle shape.

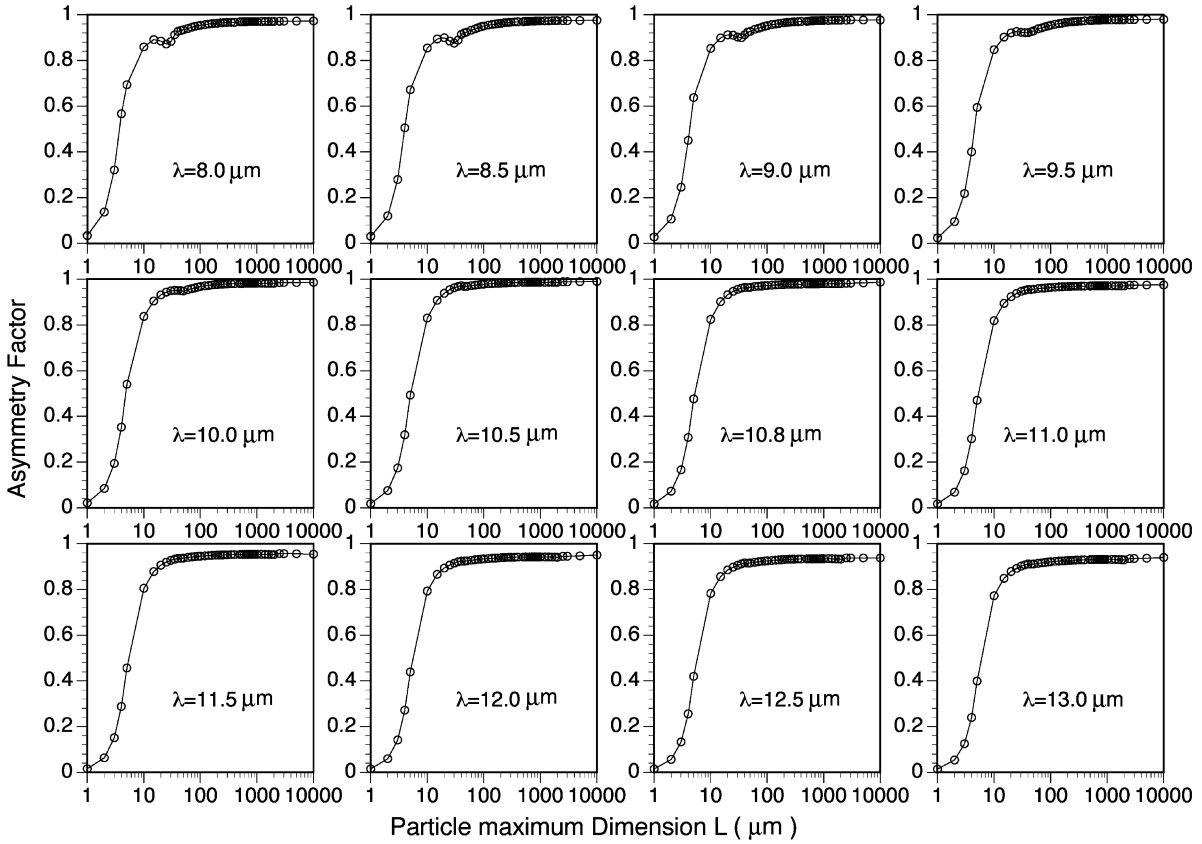

Fig. 4. The combined FDTD and IGOM solutions for the asymmetry factor at 12 wavelengths, covering particle sizes from 1 to 10,000 μm.

From Fig. 3, we note that the FDTD results and IGOM solutions converge at a particle size of 40 μm. Although the absolute amount of scattered and absorbed energy calculated by IGOM can have a substantial error for moderate particle sizes on the order of 40 μm or less, the IGOM can be used to predict the relative angular distribution of scattered energy. Thus, the normalized IGOM phase function can be a good approximation. From this physical rationale and the numerical results shown in Fig. 3, the concept of the unified theory developed by Liou et al. [22] can also be applied to the computation of the asymmetry parameter. Therefore, in this study we combine the FDTD solution (for sizes smaller than 40 μm) and IGOM results (for sizes larger than 40 μm) for the asymmetry factor so that the entire size spectrum can be covered.

Fig. 4 shows merged FDTD/IGOM results for the asymmetry factor for the 12 wavelengths for particle sizes of 1–10,000 μm. The variation of the asymmetry factor with the particle size displays a minimum at 30 μm for wavelengths 8.0, 8.5 and 9.0 μm where the absorption of ice is moderate. This minimum vanishes for longer wavelengths. The overall feature of the asymmetry parameter is that the g values are close to unity for large sizes because diffraction dominates

the scattered energy which is concentrated in forward direction. For all 12 wavelengths, there is a substantial increase in the value of the asymmetry parameter as the size of the particle increases from 1 to 40 μm. For sizes larger than 40 μm, the asymmetry parameter essentially reaches an asymptotic value.

2.3. Stretched scattering potential method for computing extinction and absorption cross sections for nonspherical particles

Several methods exist to calculate extinction and absorption cross sections for nonspherical particles. To date, the upper limit of the size parameter region for which one can obtain the exact solution for the scattering properties of certain nonspherical particles is on the order of 200. This limitation is for axisymmetrical particles such as spheroids, finite circular cylinders, and the so-called Chebyshev particles [67], as solved by the T-matrix method [68]. The applicable size parameter regimes for other exact methods to solve the scattering properties of nonspherical particles are normally smaller than that associated with the T-matrix method. For a nonaxisymmetrical particle, the size parameter region for which an exact solution may be obtained is substantially reduced. For instance, the limitation on size parameter for the T-matrix method is on the order of 40 when it is applied to hexagonal particles [A. Baran, personal communication]. The FDTD and its counterpart, the discrete dipole approximation (DDA) [69,70], encounter computational difficulties for size parameters larger than 20. For these reasons, use of an approximate method is necessary in practice. The anomalous diffraction theory (ADT) developed by van de Hulst [71] has been widely used to calculate the extinction and absorption cross sections for nonspherical particles [72–74]. Unfortunately, ADT leads to substantial errors if the refractive index of the particles is not close to 1. In particular, ADT fails to account for the tunneling effect; the absorption efficiency calculated from ADT cannot be larger than 1. The intent of this section is to derive an improved approximate method to calculate the extinction and absorption cross sections.

The wave equation derived from the Maxwell equations can be written as

$$(\nabla^2 + k^2)\bar{E}(\bar{r}) = -U(\bar{r})\bar{E}(\bar{r}), \tag{5}$$

where $U(\bar{r}) = [m^2(\bar{r}) - 1]k^2$ in which m is the complex refractive index of the medium and k is the wavenumber in a vacuum. Through comparison of Eq. (5) to the standard Schrödinger equation in quantum mechanics, we can regard $U(\bar{r})$ as a scattering potential. Thus, the light scattering problem can be treated as one concerning the interaction of photons and a potential. The separation of variables method (cf. Ref. [34]) can be used to solve Eq. (5) exactly but is limited to only a few particle shapes such as spheres and spheroids. In practice, the high-energy approximation (HEA) [75–77] and ADT can be used to solve Eq. (5) approximately. These methods are the eikonal type [78] in which rectilinear projectiles are assumed for the propagation of photons, with (or without) deviation only at the places where the scattering potential vanishes, i.e., at the particle surface. Thus, in these conventional approximations, the nonzero-interaction region is where wave function undergoes phase delay and absorption and is limited inside the particle. Recently, Fu et al. [30] have computed the Poynting vector for the near-field associated with the scattering of IR radiation by a hexagonal ice crystal to illustrate

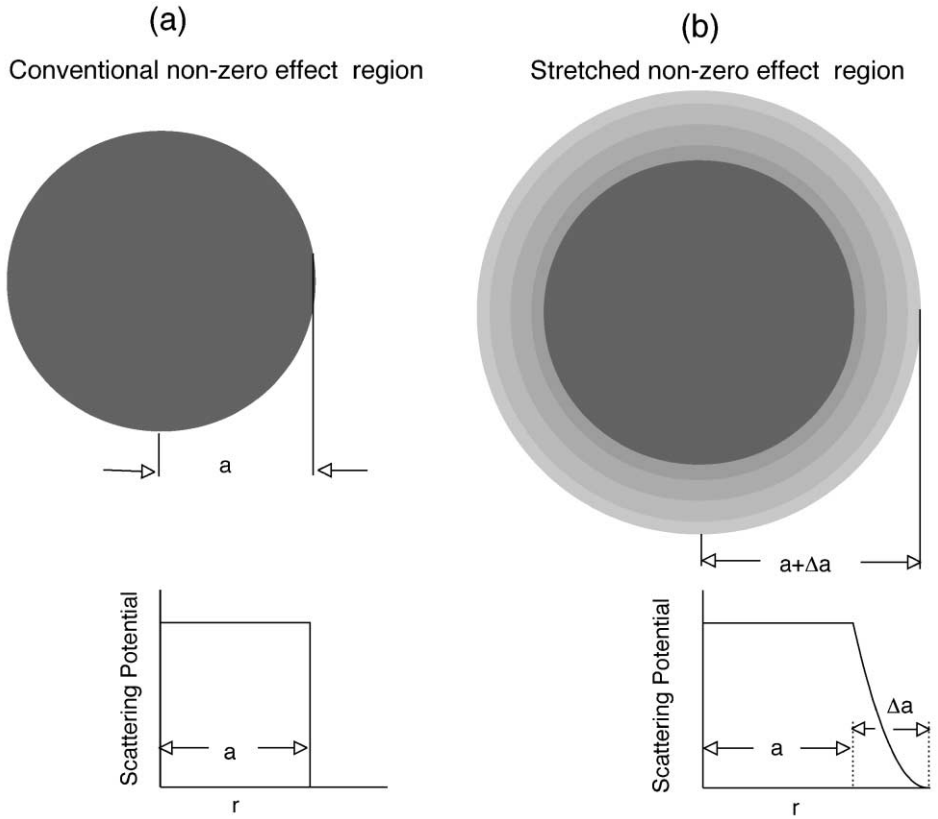

Fig. 5. Conceptual diagrams of the spherical particle case illustrating the principle of the conventional eikonal-type approximation and the present stretching scattering potential method (SSPM): (a) the nonzero effect region for phase delay and wave attenuation in the conventional method. The radius of the sphere is denoted by a; (b) the region of nonzero scattering potential in the SSPM. The scattering potential is expanded outside the particle in the region between a and $a + \Delta a$ to account for the tunneling effect.

the flow of electromagnetic energy around the particle. It is shown that the incident Poynting stream outside the geometric projected area of the particle can deviate and be traced through the particles, a phenomenon otherwise known as the tunneling or the above-edge effect. Although HEA and ADT provide a good physical insight in concept and a simple mathematical formulation in practice, they may produce significant errors in computation, e.g., a substantial underestimation of absorption efficiency in the resonance region because of the failure to account for the tunneling effect.

To avoid this shortcoming of the conventional eikonal-type approximation that is applied to solve Eq. (5), it is necessary to stretch the scattering potential to account for the tunneling effect. Fig. 5(a) illustrates the region of non-null scattering potential, where the interaction of photons and medium occurs for the conventional eikonal methods. The scattering potential $U(\bar{r})$ is nonzero only inside the particles for the conventional methods. Fig. 5(b) is the conceptual diagram for the present stretched scattering potential method (SSPM), where a is the physical

size of the particle and Δa is extension for the stretched potential. In this method, the scattering potential $U(\bar{r})$ is stretched so that the nonzero effect region for photon propagation extends outside the physical volume of the scattering particle. We assume the scattering potential has a quadratic distribution, for example, in the spherical particle case, as follows:

$$U(r) = \begin{cases} (m^2-1)k^2, & r \leqslant a, \\ (m^2-1)k^2[1-(r-a)/\Delta a]^2, & a < r \leqslant a+\Delta a, \\ 0, & r \geqslant a+\Delta a. \end{cases} \tag{6}$$

For stretched scattering potential in the region between a and $a+\Delta a$, we can define an effective refractive index $\tilde{m} = (\tilde{m}_r + i\tilde{m}_i)$ given by

$$\tilde{m}^2 - 1 = (m^2-1)[1-(r-a)/\Delta a]^2. \tag{7}$$

The solution of Eq. (7) is

$$\alpha = 1 + (m_r^2 - m_i^2 - 1)[1-(r-a)/\Delta a]^2, \tag{8a}$$

$$\beta = m_r m_i [1-(r-a)/\Delta a]^2, \tag{8b}$$

$$\tilde{m}_r(r) = [\alpha + (\alpha^2 + 4\beta^2)^{1/2}]/2 \quad \text{and} \tag{8c}$$

$$\tilde{m}_i(r) = \beta/\tilde{m}_r(r). \tag{8d}$$

The external reflection and multiple internal reflections and subsequent transmission of the wave is completely neglected in the conventional eikonal-type approximate methods to solve Eq. (5). The result of ignoring these effects is equivalent to an overestimation of scattering potential. To include the external and internal reflection/transmission effect equivalently, the scattering potential should be compressed instead of being stretched.

The compressed scattering potential is given in the form of

$$U(r) = \begin{cases} (m^2-1)k^2, & r \leqslant a-\Delta a, \\ (m^2-1)k^2[1-(r-a+\Delta a)/\Delta a]^2, & a-\Delta a < r \leqslant a, \\ 0, & r \geqslant a. \end{cases} \tag{9}$$

Fig. 6 shows the concept of using an eikonal approximation in the ADT framework to calculate the extinction and absorption cross sections for a spherical particle. In practice, continuous variation of the effective refractive index is discretized as various layers. That is, the effect of stretching the scattering potential is equivalent to adding some dielectric medium layers outside the scattering particle. For a given layer, we calculate the mean effective refractive index as follows:

$$\langle \tilde{m}_r + i\tilde{m}_i \rangle_j = \frac{1}{\Delta r} \int_{r_j-\Delta r/2}^{r_j+\Delta r/2} [\tilde{m}_r(r) + i\tilde{m}_i(r)\,\mathrm{d}r, \tag{10}$$

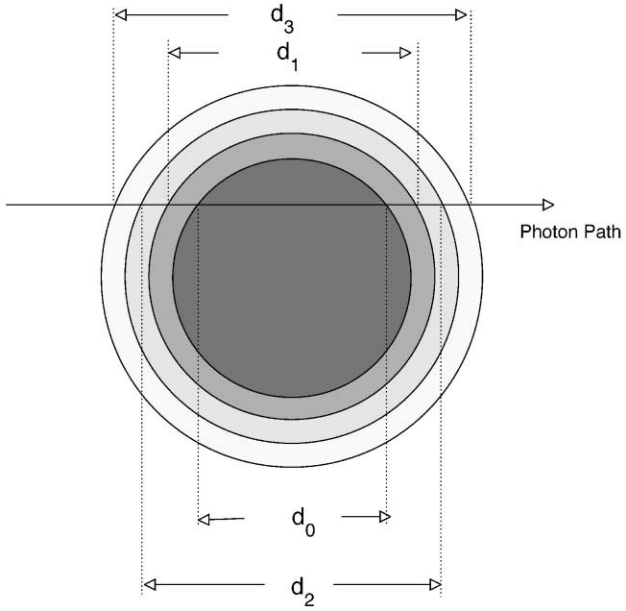

Fig. 6. Conceptual diagram illustrating the computational scheme for a multi-layered particle in the frame of an eikonal-type approximate method. Rectilinear projectiles are assumed for the photon paths in conjunction with the computation of phase delay and wave attenuation.

where r_j is the radius of the jth layer and Δr is the thickness of the layer. A uniform thickness is assumed for all the layers in the present study. According to the geometry shown in Fig. 6 and the physical assumption in conjunction with Huygen's principle for the ADT approximation [71], we obtain expressions for the extinction cross section (σ_{ext}) and the absorption cross section (σ_{abs}) for a layered sphere, respectively, as follows:

$$\sigma_{\text{ext}} = 2 \iint_P (1 - \mathrm{e}^{-\gamma} \cos\rho)\, \mathrm{d}^2 P, \tag{11a}$$

$$\sigma_{\text{abs}} = \iint_P (1 - \mathrm{e}^{-2\gamma})\, \mathrm{d}^2 P, \tag{11b}$$

where the domain of the integration, P, is the projected area of the particle, and ρ is the phase delay that a photon undergoes in conjuction with its penetration of the multilayered sphere. The phase delay parameter is given by

$$\rho = kd_0(m_r - 1) + \sum_{j=1}^{N} k(d_j - d_{j-1})(\langle \tilde{m}_r \rangle_j - 1), \tag{11c}$$

in which d_0 is the length of the photon projectile inside the particle and d_i is the length of photon path inside the ith layer, as is shown in Fig. 6. In Eq. (11c) N is the number of total

layers outside the particle. The attenuation factor, γ, for the damping of the incident wave is given by

$$\gamma = kd_0 m_i + \sum_{j=1}^{N} k(d_j - d_{j-1})\langle \tilde{m}_i \rangle_j. \tag{11d}$$

Eqs. (11c) and (11d) are for the case where the scattering potential is stretched outside the particle. A similar mathematical formulation may be derived for the case when the scattering potential is compressed or reduced.

From the preceding discussion of the SSPM approximation, the only tuning parameter is the distance Δa for stretching the scattering potential. The physical processes associated with the extinction and absorption of the incident wave are quite different. For example, the surface wave (a term in the rigorous physical picture) [43,71] that creeps along the particle surface can contribute to the extinction but not to the absorption. This is because the surface waves do not enter the interior of the particle (i.e., they do not undergo absorption), but are responsible for large angle diffraction, as is illustrated by Mitchell [44]. Note that diffraction is a part of extinction process. Therefore, the magnitude of the extension of the scattering potential may be different for calculating the extinction cross section from calculating the absorption cross section. For this reason, we denote Δa as Δa_e and Δa_a for extinction and absorption calculations, respectively.

Fig. 7 shows the values of Δa_e that are derived from the best fit of the exact Mie solution using the SSPM results in the spherical case. In this study, the computational Mie code developed by Wiscombe [79] is used. To determine Δa_e, a Mie calculation is first carried out; subsequently a Monte Carlo method is employed to determine the proper value for Δa_e for the SSPM method. Specifically, for each SSPM calculation in the case where the potential is stretched rather than compressed, we chose

$$\Delta a_e = \xi a, \tag{12}$$

where ξ is a random number that is uniformly distributed in $[0, 1]$. From Fig. 7, it is shown that the magnitude of Δa_e increase with particle dimension. However, the ratio of Δa_e to the particle dimension reaches a maximum at a particle size of approximately 10 μm where the resonance effect is largest. As is evident in Fig. 7, the SSPM extinction efficiency actually overlaps with the Mie solution. If the procedure for calculating Δa_e and the extinction efficiency were reversible, the SSPM could reproduce the exact theory, providing that adequate extension of the scattering potential was known a priori. It is straightforward to obtain the correct stretching scattering potential for the SSPM calculation for a spherical particle case because of the availability of the exact Mie theory, as is evident from the results shown in Fig. 7. For scattering by a nonspherical particle, it is necessary to define an approximation of the correct expansion of the scattering potential.

Fig. 8 is similar to Fig. 7 except it relates to the absorption calculation. Again, if Δa_a is properly selected, the SSPM result can match the analytical Mie solution. Another feature of the behavior of Δa_a as a function of the particle size is that negative values are noted for very large particles. This means that the scattering potential should be compressed in the calculation of

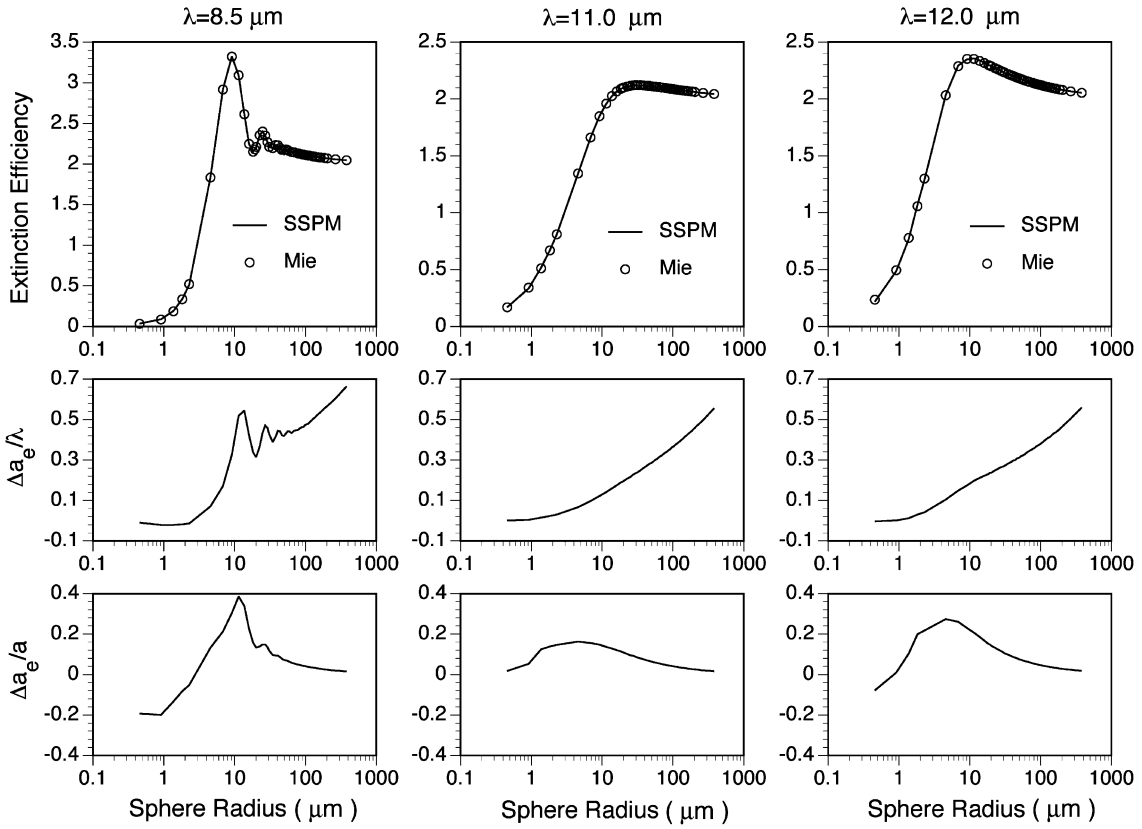

Fig. 7. The expansion parameter Δa_e derived from the best fit of the SSPM solutions to the exact Mie results for the spherical case at wavelengths 8.5, 11.0, and 12.0 μm. The values of SSPM extinction efficiency corresponding to the best fitting Δa_e are also shown in comparison with the Mie results in the top row. The parameter Δa_e are presented in an absolute scale (in the unit of incident wavelength) in the middle row. The percentage of Δa_e with respect to the particle radii is shown in the bottom row.

absorption cross section because the effect of external reflection and refraction is not accounted for in the eikonal-type approximation given by Eqs. (11a)–(11d). For the absorption efficiency at 12.0 μm wavelength, a pronounced tunneling effect can be observed because the absorption efficiency is substantially larger than unity for particle sizes near 10 μm. The SSPM accounts for the tunneling effect, providing a proper expansion of the scattering potential is used.

It is problematic to accurately predescribe the expansion of the scattering potential for SSPM calculation for a nonspherical particle. In this case, we approximate Δa_e and Δa_a by the values obtained from the equivalent spheres with radii defined by Eq. (4) that conserves both the volume and projected-area in the equivalence process. In the SSPM computation for hexagonal ice crystals, we specifically solve for the phase delay and wave attenuation for a number of layered hexagons. The total number of the hexagonal layers and their thicknesses are approximated by their counterparts in the spherical case. Fig. 9 is a conceptual flow chart for determining the

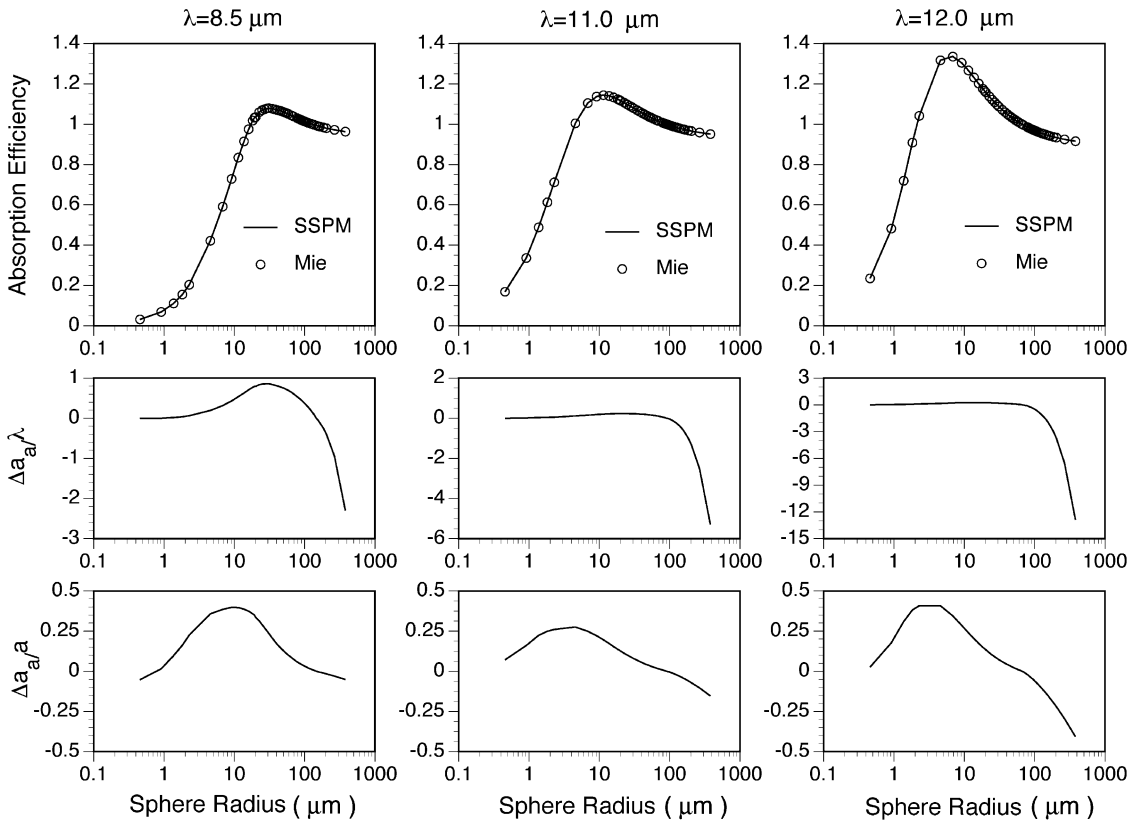

Fig. 8. The same as Fig. 7 except for absorption efficiency. A pronounced tunneling effect is evident at the 12.0 μm wavelength, as the absorption efficiency is substantially larger than unity at particle radii near 10 μm.

three-dimensional geometry including the region of stretched scattering potential for nonspherical particle for SSPM calculation. As shown in Fig. 9, we first determine the parameter Δa_e (or Δa_a) for the equivalent sphere by matching the SSPM calculation (in spherical case) with the corresponding Mie solution. Subsequently, the stretching parameter Δa_e that is obtained for the equivalent sphere is used as a surrogate for nonspherical ice crystals. Evidently, nonsphericity effect is explicitly accounted for in SSPM calculation for ice crystals.

Fig. 10 shows the absorption efficiency of hexagonal ice crystals calculated from various methods. The errors of the FDTD results are less than 1% for the typical grid resolution [40]. Thus, the FDTD results here can be used as a reference for checking the accuracy of the approximate methods. As shown in Fig. 10, the SSPM results essentially overlap with the FDTD solution for wavelengths of 8.0, 8.5, 9.0, 9.5, 10.0, and 10.5 μm. For longer wavelengths, deviation of the SSPM results from FDTD is noted for particle sizes larger than 20 μm. It also becomes evident that the GOM, ADT, and MTFES may lead to substantial errors. In particular, ADT will significantly overestimate the absorption efficiency for very large particles when the particles are strongly absorptive at a given wavelength. The asymptotic value for ADT absorption

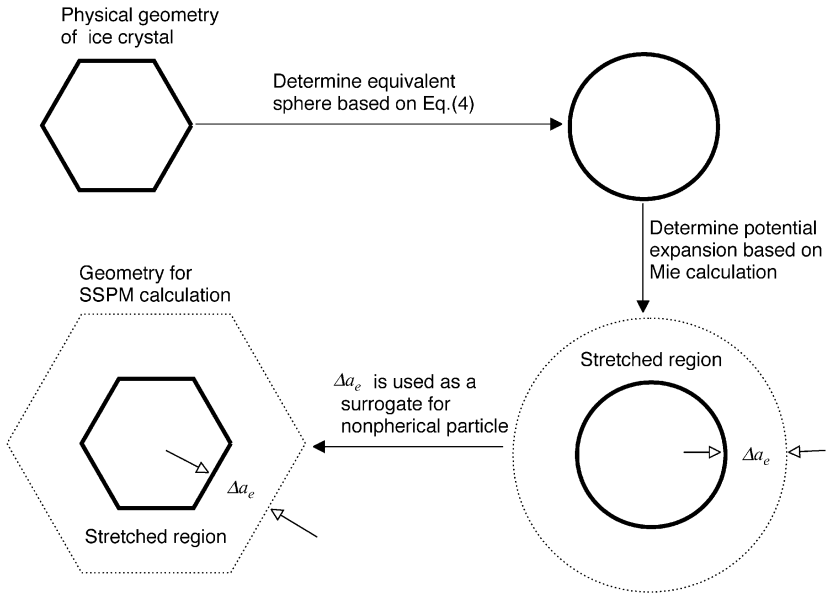

Fig. 9. A flow chart illustrating the procedure for determining the stretching parameter Δa_e. Note that Δa_a for the absorption calculation can be determined in the same manner.

efficiency is unity because the external reflection is unaccounted for in this approximation. The Mie results shown in Fig. 10 are generated for spheres whose radii are defined by Eq. (4).

Fig. 11 is similar to Fig. 10 except that results are shown for extinction efficiency. One obvious result is that Mie theory for the equivalent spheres substantially overestimates the extinction at the resonance maximum. The GOM and ADT methods converge for large particles. The GOM results shown here are from the improved geometric optics method developed by Yang and Liou [41,42]. If the conventional ray tracing method is used, the extinction efficiency is simply 2 regardless of particle size, as is pointed out by Yang and Liou [35]. For all 12 wavelengths the SSPM results seem to provide the most consistent comparisons with the FDTD method.

Some physical processes, such as the external reflection and detailed nonsphericity effects, are not fully accounted for in the SSPM because exact expansion of the potential is not used. The effects associated with these physical processes are reflected in the equivalent Mie and GOM results to some extent. Thus, we can refine the SSPM results as follows:

$$Q_{\text{refined}} = (1 - \delta_1 - \delta_2)Q_{\text{SSPM}} + \delta_1 Q_{\text{Mie}} + \delta_2 Q_{\text{GOM}}, \tag{13}$$

where Q stands for either extinction efficiency Q_e or absorption efficiency Q_a. The values of the parameters δ_1 and δ_2 are so determined that the Q_{refined} best fit the FDTD results for crystal sizes between 20 and 40 μm. It is found that the parameters δ_1 and δ_2 in Eq. (3) are strongly dependent on wavelength. For example, the weighting coefficients for the SSPM,

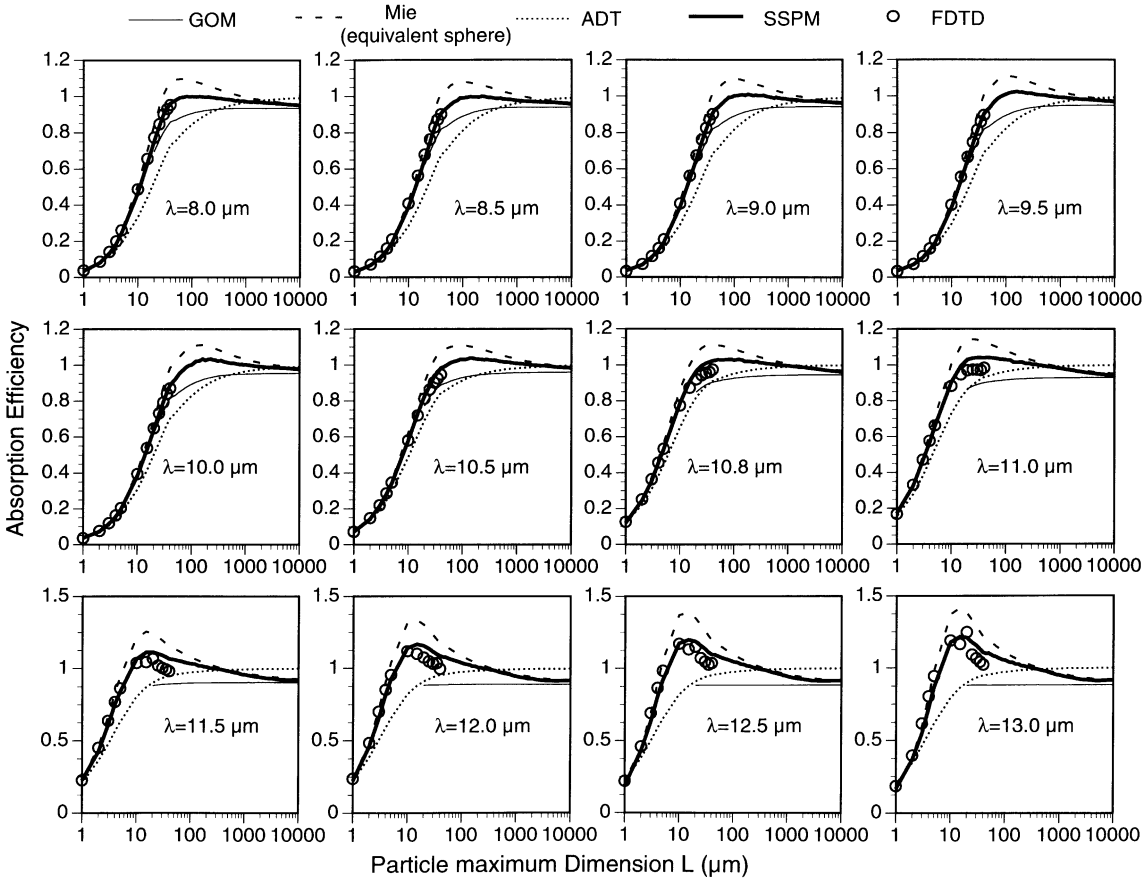

Fig. 10. The absorption efficiency of hexagonal ice crystals computed from various methods. The particle sizes are defined by their maximum dimensions with an implicit inclusion of aspect ratio defined in Eq. (1). The expansion parameter Δa_e and Δa_a required for SSPM calculation in the hexagonal case are approximated by their counterparts in a spherical case, that is, the number of layers of stretched potential and their thickness in hexagonal case is the same as in the spherical case.

Mie, and GOM solutions in Q_a calculation are $(1-\delta_1-\delta_2, \delta_1, \delta_2) = (0.186, 0.2036, 0.6104)$ and $(0.6641, 0.0042, 0.3317)$ for 10.5 and 12.5 μm, respectively. The corresponding values for Q_e calculation are $(0.6880, 0.0, 0.3120)$ and $(0.6160, 0.0004, 0.3836)$. The refined SSPM results are given only for sizes larger than 20 μm, because the geometric optics solution involved in Eq. (13) is essentially meaningless due to the failure of the localization principle for small size parameters. Fig. 12 shows the refined SSPM results for the extinction and absorption cross section efficiencies. With this refinement, calculations can be provided for the entire size spectrum. The refinement procedure employed here is similar to that used by Fu et al. [29] who use a weighted summation of Mie and IGOM solutions to obtain an approximate fit for the single-scattering properties of hexagonal ice crystals.

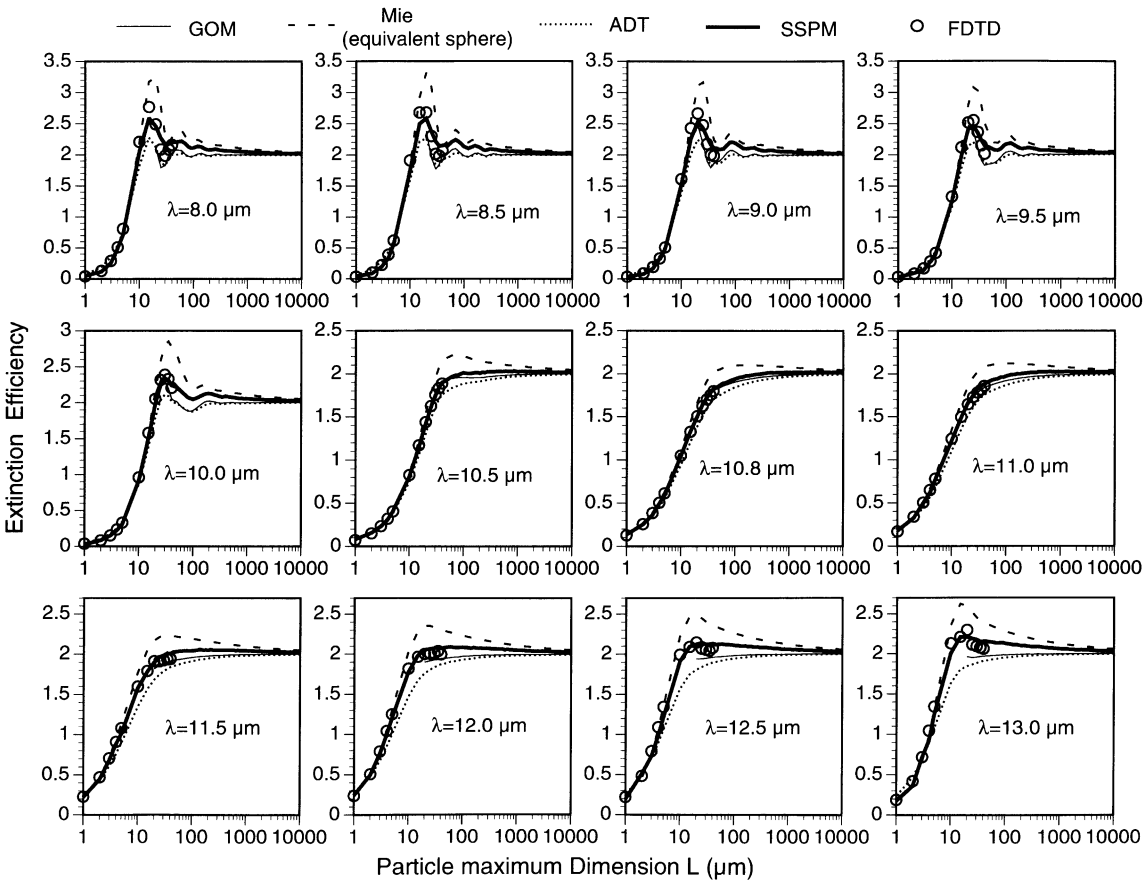

Fig. 11. The same as Fig. 10 except for extinction efficiency.

3. Application to cirrus clouds and parameterizations

To derive a set of ice crystal bulk scattering properties for practical applications, it is necessary to derive the single-scattering properties using realistic particle size distributions. In this study, we select the 28 size distributions used by Fu [28] with an additional two datasets from Mitchell et al. [80]. These size distributions were measured for a variety of midlatitude and tropical cirrus clouds and were obtained during various field campaigns including the Central Equatorial Pacific Experiment (CEPEX) [81]. McFarquhar et al. [82] showed that the microphysical properties of ice crystals for tropical cirrus clouds are quite different from those for midlatitude cirrus systems.

It is common to characterize the bulk properties of a size distribution by two parameters—ice water content (IWC) and effective size. For a given size distribution, IWC is defined as follows:

$$IWC = \rho_{\text{ice}} \int_{L_{\min}}^{L_{\max}} V(L) n(L)\, \mathrm{d}L, \tag{14}$$

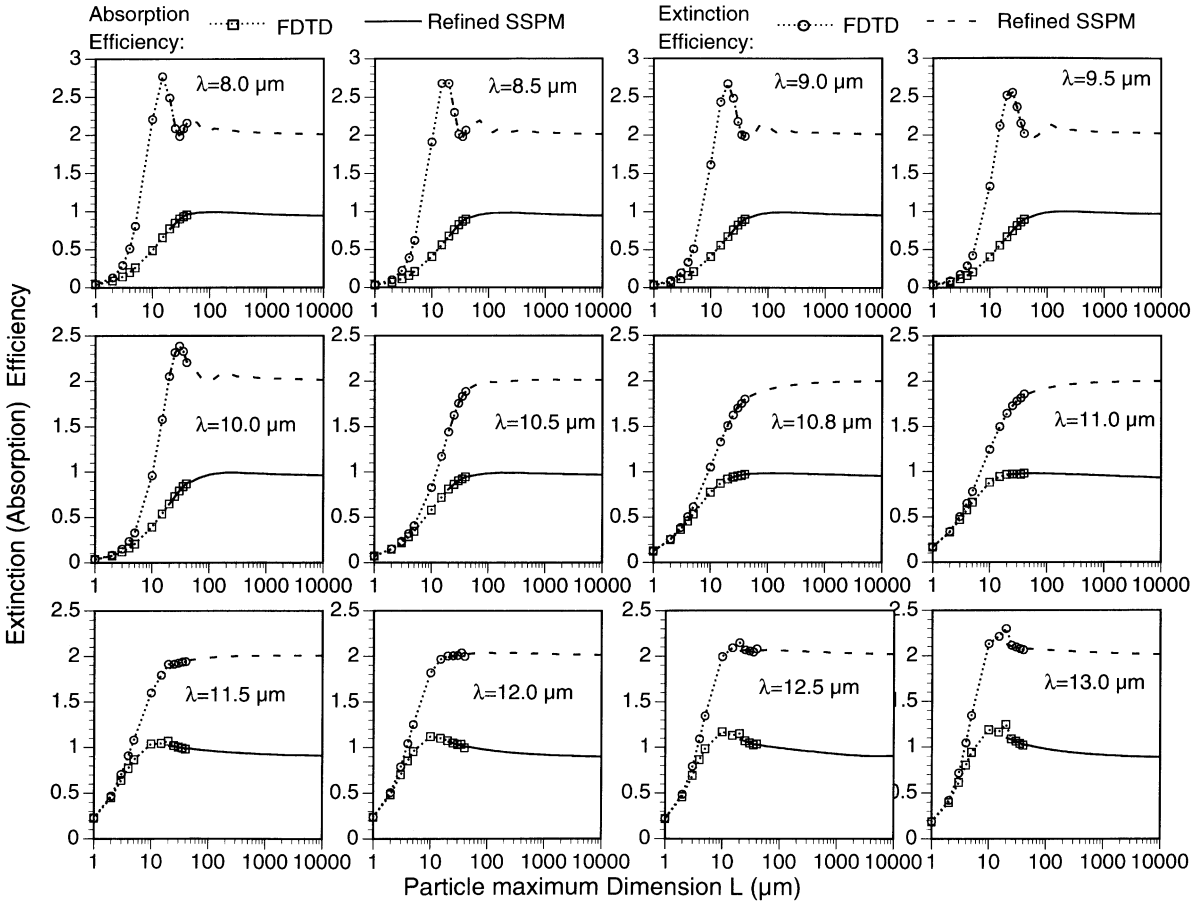

Fig. 12. The combination of the FDTD and refined SSPM results for the absorption and extinction efficiency for the particle sizes ranged from 1 to 10,000 μm. A smooth transition between the two methods is evident for both of the efficiencies.

where ρ_{ice} is the mass density of bulk ice, $n(L)$ is particle number density, $V(L)$ is the volume of an ice crystal at bulk ice density with maximum dimension of L, and $L_{\min}$ and $L_{\max}$ are the minimum and maximum sizes in the size distributions, respectively. There are many definitions for effective size in the literature. Wyser and Yang [31] performed a comprehensive comparison of definitions commonly used in different parameterization efforts. In this study, we define the effective size following Foot [83], Francis et al. [5], Fu [28], Wyser and Yang [31], and Grenfell and Warren [66] as

$$D_{\text{e}} = \frac{3}{2}\frac{\int_{L_{\min}}^{L_{\max}} V(L)n(L)\,\mathrm{d}L}{\int_{L_{\min}}^{L_{\max}} A(L)n(L)\,\mathrm{d}L}, \tag{15}$$

where $A(L)$ is the projected-area of the particle with size of L. The preceeding definition reduces to that defined by Hansen and Travis [84] for spherical particles. We note that Eq. (15) is similar

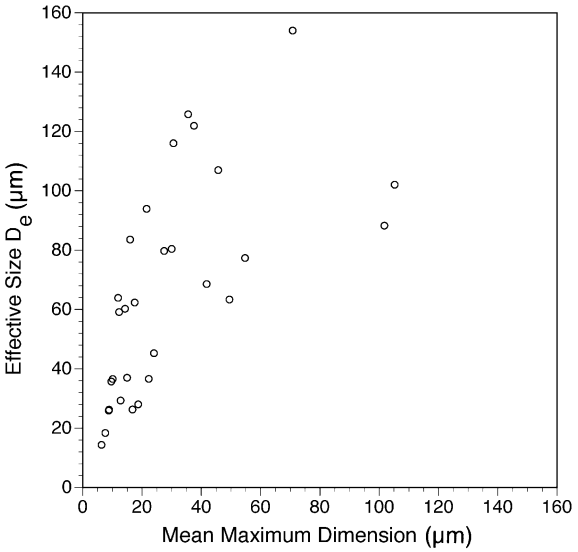

Fig. 13. A scatterplot demonstrating the relationship between the effective sizes and mean maximum dimensions computed for the 30 size distributions from Fu (Ref. [28]) and Mitchell et al. (Ref. [80]).

to Eq. (4) except that only an individual particle is considered in Eq. (4) whereas Eq. (15) considers a size distribution. In addition to the effective size, we also define the mean maximum dimension for a given size distribution as follows:

$$\langle L\rangle = \frac{\int_{L_{\min}}^{L_{\max}} Ln(L)\,\mathrm{d}L}{\int_{L_{\min}}^{L_{\max}} n(L)\,\mathrm{d}L}. \tag{16}$$

Fig. 13 shows a scatterplot for the effective size D_e as a function of the mean maximum dimension $\langle L\rangle$ for the aforementioned thirty size distributions described. It is evident that D_e is normally larger than $\langle L\rangle$ for a given size distribution. This occurs because the distributions contain a large number of small particles that are significant in defining the mean maximum dimension. However, the contribution of small particles to the total volume or projected-area is relatively small regardless of their contribution . Thus, the largest weight in defining D_e is for moderate or large ice crystals. It is also evident from Fig. 13 that the spectrum of effective sizes ranges from approximately 10 to 160 μm for the selected size distribution datasets. Given the range of effective sizes, the present set of ice cloud size distributions should provide an effective basis for a parameterization effort. It is worth noting that D_e depends on ice crystal shapes and sizes when $\langle L\rangle$ is held constant.

For a given size distribution of ice crystals, the bulk extinction coefficient is defined as follows:

$$\beta_e = \int_{L_{\min}}^{L_{\max}} Q_e(L)A(L)n(L)\,\mathrm{d}L. \tag{17}$$

It is convenient in practice to define a volume-normalized extinction coefficient [31], given by

$$\tilde{\beta}_e = \frac{\beta_e}{(IWC/\rho_{ice})} = \frac{\int_{L_{min}}^{L_{max}} Q_e(L)A(L)n(L)\,dL}{\int_{L_{min}}^{L_{max}} V(L)n(L)\,dL}. \tag{18}$$

Note that the quantity (IWC/ρ_{ice}) in the preceeding equation provides the total bulk volume of ice crystals for a given size distribution. For a cirrus cloud with a given IWC and geometrical thickness Δz, the dimensionless optical thickness of the cloud may be obtained from

$$\tau = \tilde{\beta}_e \frac{IWC}{\rho_{ice}} \Delta z. \tag{19}$$

This relationship is useful in practice because IWC is now a prognostic parameter in many global climate models (GCMs) [85]. In many parameterization efforts, it is common to parameterize β_e or $\tilde{\beta}_e$ as a function of the effective size. In particular, it has been found that the extinction coefficient decreases with an increase in effective size (e.g., Refs. [28,31]). We suggest that it may be more useful to parameterize the mean extinction efficiency rather than the extinction coefficient. The volume-normalized extinction coefficient $\tilde{\beta}_e$ can be rewritten exactly as

$$\tilde{\beta}_e = \frac{3}{2D_e}\langle Q_e \rangle, \tag{20}$$

where $\langle Q_e \rangle$ is the mean extinction efficiency that is defined as

$$\langle Q_e \rangle = \frac{\int_{L_{min}}^{L_{max}} Q_e(L)A(L)n(L)\,dL}{\int_{L_{min}}^{L_{max}} A(L)n(L)\,dL}. \tag{21}$$

From inspection of Eqs. (20) and (21), we suggest that the accuracy of a parameterization scheme would be improved if the mean extinction efficiency could be parameterized accurately.

For visible wavelengths, the size parameter is very large even for small ice crystals on the order of 10 μm. Thus, for visible wavelengths, the extinction efficiency of an ice crystal essentially approaches a geometric optics asymptotic value of 2 for a realistic set of particle sizes. For the IR region of interest in the present study, the resonance effect is obvious for ice crystal sizes between 10 and 20 μm. However, the number concentration of particles in this size region may be significant for some ice clouds such as contrails and cold cirrus. Thus, $\langle Q_e \rangle$ needs to be investigated carefully in a parameterization effort. From Eq. (20), the wavelength-dependent part of the extinction coefficient is the mean extinction efficiency. The mean extinction efficiency can be parameterized as a function of effective size.

Fig. 14 shows the variation of the volume-normalized extinction coefficient, $\tilde{\beta}_e$, as a function of effective size for 12 wavelengths in the IR window region. The extinction coefficient decreases with an increase of effective particle size, as expected from Eq. (20). For effective particle sizes larger than 80 μm, the extinction coefficient approaches its asymptotic value with a small variation as particle size increases. We note that $\tilde{\beta}_e$ can be regarded as the extinction coefficient for a unity IWC because the mass density of ice is independent of the size distribution. For a

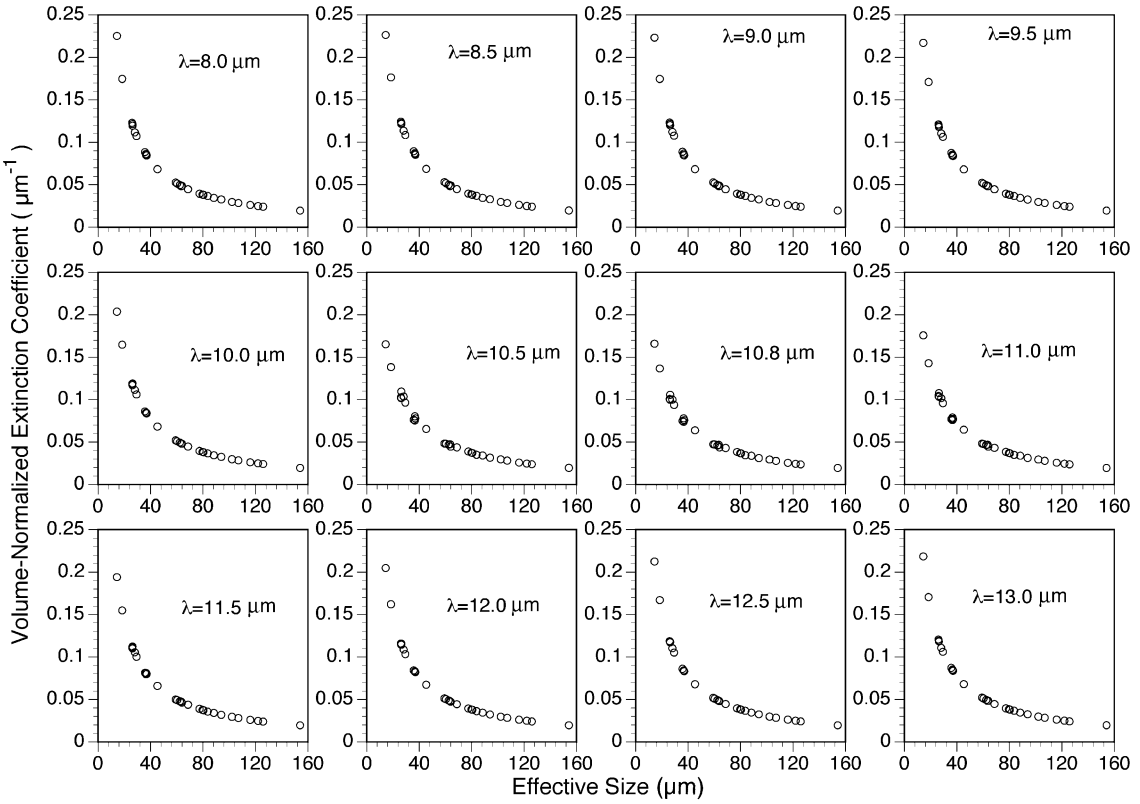

Fig. 14. The variation of the volume-normalized extinction coefficient versus the effective size for 12 wavelengths in the IR window region.

fixed cloud geometrical thickness and *IWC*, according to Fig. 14 and Eq. (19), the cloud will have a larger optical thickness if the ice crystals are small. Conversely, the optical thickness of the cloud will be reduced if the particle sizes are large.

The circle symbols in Fig. 15 show the variation of the dimensionless mean extinction efficiency as a function of $1/D_e$. The variation pattern of $\langle Q_e \rangle$ is shown to have a dependence on wavelength. The magnitude of $\langle Q_e \rangle$ ranges between 1.5 and 2.2. When $1/D_e$ approaches zero (i.e., large effective size), the mean effective extinction efficiency is close to 2. This is expected because the particle extinction efficiency reaches its geometric optics asymptotic value when the size is very large. For wavelengths $8.5, 9.0, 9.5, 10.0, 12.0, 12.5$ and $13.0\ \mu m$, an extinction maximum is observed for the moderate effective sizes. For wavelengths 10.5, 10.8, 11.0, and 11.5 μm near the Christiansen band, the mean extinction efficiency decreases with the increase of $1/D_e$, i.e., a decrease of particle mean size.

The mean extinction efficiency may be parameterized by a second-order polynomial in the form of

$$\langle Q_e \rangle = \eta_2 (1/D_e)^2 + \eta_1 (1/D_e) + \eta_0, \tag{22}$$

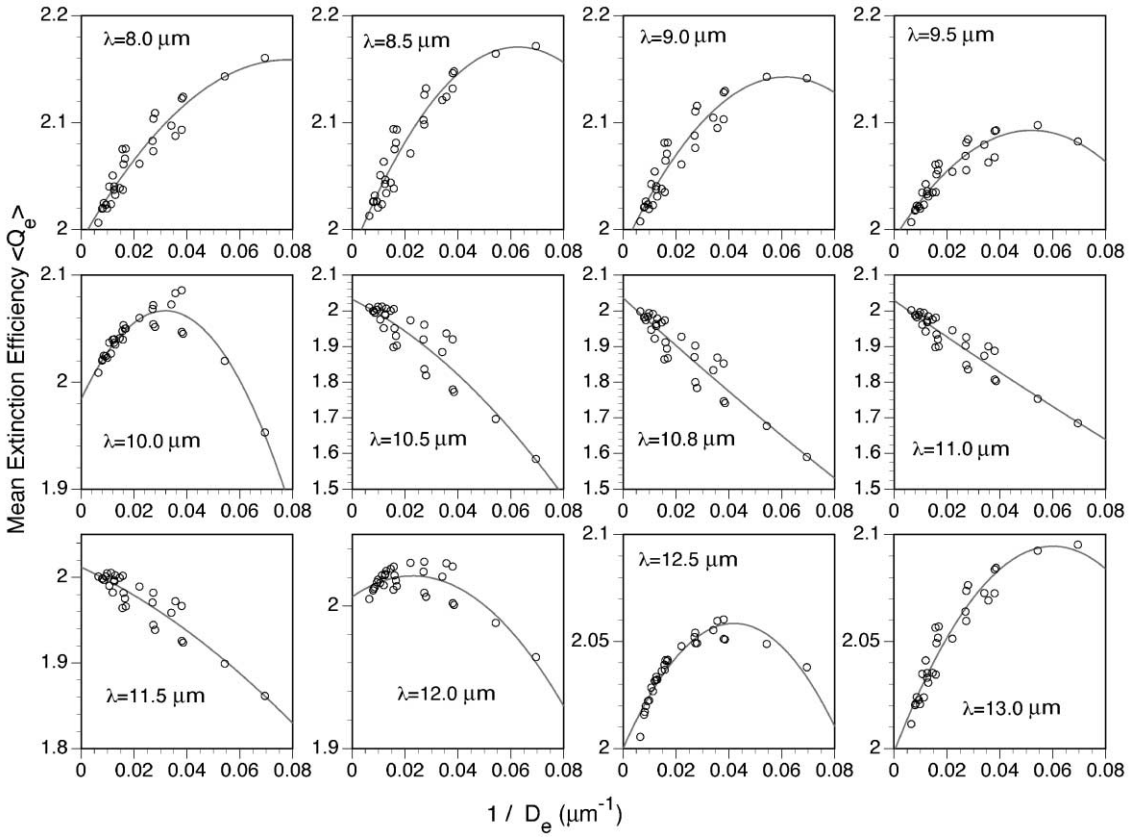

Fig. 15. The mean extinction efficiency calculated for the 30 size distributions (circle symbols). The solid lines are the parameterization results obtained from fitting the "exact" data in terms of the second order polynomial function of $1/D_e$.

where the coefficients η_0, η_1, and η_2 are determined from the least-squared fitting technique. Table 1 lists the three fitting coefficients derived for the 12 wavelengths. The parameterization results are also shown in Fig. 15 (solid lines).

The circle symbols in Fig. 16 show the a variation of single-scattering albedo with $1/D_e$. Here the mean value of the single-scattering albedo for a given size distribution is defined as follows:

$$\langle\tilde{\omega}\rangle = \frac{\int_{L_{\min}}^{L_{\max}} [Q_e(L) - Q_a(L)]A(L)n(L)\,dL}{\int_{L_{\min}}^{L_{\max}} Q_e(L)A(L)n(L)\,dL}. \tag{23}$$

The overall variation trend of $\langle\tilde{\omega}\rangle$ in the IR window region can be grouped into two categories: for wavelengths smaller than 10.0 μm, the single-scattering albedo increases with an increase of $1/D_e$, i.e., single-scattering albedo increases with decreasing mean particle size; for wavelengths

Table 1
The fitting coefficients for the parameterization of the mean extinction efficiency, which is defined by the Eq. (22)

Wavelength (μm)	η_0	η_1	η_2
8.0	1.989	4.336	−2.776E + 1[a]
8.5	1.979	6.117	−4.877E + 1
9.0	1.982	5.219	−4.248E + 1
9.5	1.992	3.891	−3.743E + 1
10.0	1.984	5.208	−8.194E + 1
10.5	2.032	−3.643	−4.075E + 1
10.8	2.036	−6.777	5.749
11.0	2.029	−5.179	3.789
11.5	2.012	−1.431	−1.061E + 1
12.0	2.006	1.283	−2.800E + 1
12.5	2.000	2.787	−3.323E + 1
13.0	1.998	3.201	−2.664E + 1

[a]Read 2.776E + 1 as $2.776 \times 10^{+1}$.

Table 2
The fitting coefficients for the parameterization of the mean single-scattering albedo, which is defined by the Eq. (24)

Wavelength (μm)	ζ_0	ζ_1	ζ_2
8.0	5.294E − 1	2.536E − 1	1.541E + 1
8.5	5.205E − 1	1.421	7.036
9.0	5.198E − 1	1.178	9.676
9.5	5.191E − 1	1.040	1.063E + 1
10.0	5.116E − 1	1.770	−1.811
10.5	5.230E − 1	−8.619E − 1	1.271
10.8	5.384E − 1	−2.454	1.225E + 1
11.0	5.475E − 1	−2.552	1.417E + 1
11.5	5.562E − 1	−1.974	9.011
12.0	5.633E − 1	−1.919	9.232
12.5	5.556E − 1	−1.605	7.246
13.0	5.678E − 1	−2.051	1.237E + 1

longer than 10.5, the opposite behavior is observed. A second-order polynomial function may be employed to fit the single-scattering albedo in the form of

$$\langle\tilde{\omega}\rangle = \zeta_2(1/D_e)^2 + \zeta_1(1/D_e) + \zeta_0. \tag{24}$$

Table 2 lists the fitting coefficients in Eq. (24). The solid lines in Fig. 16 show the corresponding parameterization results.

The circle symbols in Fig. 17 show the asymmetry factor calculated for the 30 size distributions at 12 wavelengths. In this figure, the asymmetry factor is plotted against the effective size rather than against $1/D_e$ as in Figs. 15 and 16. The asymmetry factor increases with an increase in the effective size. One explanation for this is that particle absorption reduces the amount of scattered energy in the side scattering and back scattering directions, and affects the transmission of the incident wave. In addition, the diffracted energy is concentrated in a narrower region around the forward scattering direction when the particle sizes are increased.

While polynomial functions are employed often to parameterize the asymmetry factor (e.g., Refs. [28,31]), we suggest instead the use of a power-law form, which may be mathematically expressed as follows:

$$\langle g\rangle = \varsigma(\langle D_e\rangle)^{\kappa}. \tag{25}$$

The fitting coefficients ς and κ for Eq. (25) are listed in Table 3. Our parameterization results as given by Eqs. (22), (24) and (25) should be limited to the domain of effective sizes (approximately 10–160 μm) used in our analyses. For an effective size outside of this range, the applicability of the parameterization should be checked discreetly to avoid any unpleasant artifacts.

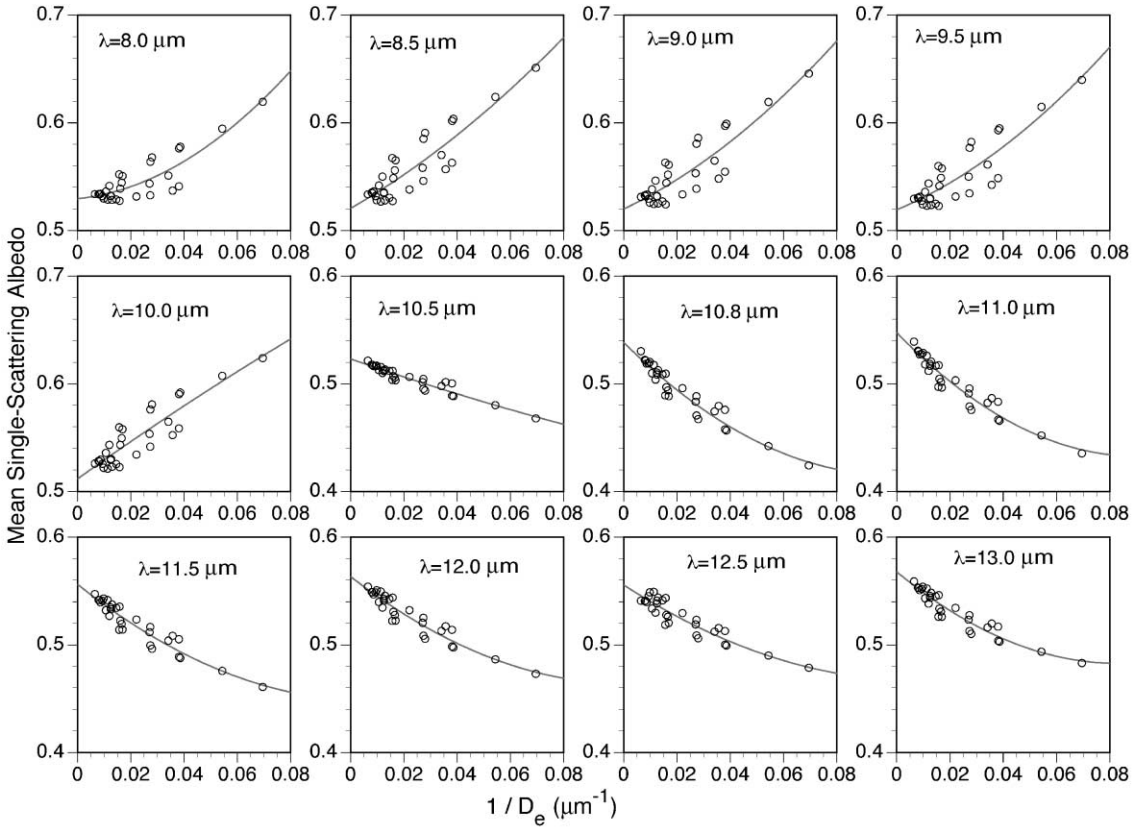

Fig. 16. The same as Fig. 15 except for mean single-scattering albedo. An increasing trend is evident for the variation of the single-scattering albedo versus $1/D_e$ at wavelengths 8.0, 8.5, 9.0, 9.5 and 10.0 μm. A decreasing trend is noted for the other wavelengths.

4. Conclusions

We present fundamental scattering and absorption properties for hexagonal ice crystal columns with sizes ranging form 1 to 10,000 μm in the infrared (IR) 8–13 μm window region. The 8–13 μm region contains a wealth of spectral information that may be beneficial for satellite-borne IR retrieval of ice cloud properties. To obtain scattering and absorption properties over this range of particle sizes, two method need to be employed because there is currently no single-scattering computational method that can cover the entire size parameter spectrum. In this study we use the finite-difference time domain (FDTD) method to solve for the extinction efficiency, single-scattering albedo, and the asymmetry parameter of the phase function for ice crystals smaller than 40 μm. We find that the improved geometric optics method (IGOM) can be employed to calculate the asymmetry parameter for ice crystals larger than 40 μm if one accounts for the inhomogeneity effect of the refracted wave inside the nonspherical ice particle. The

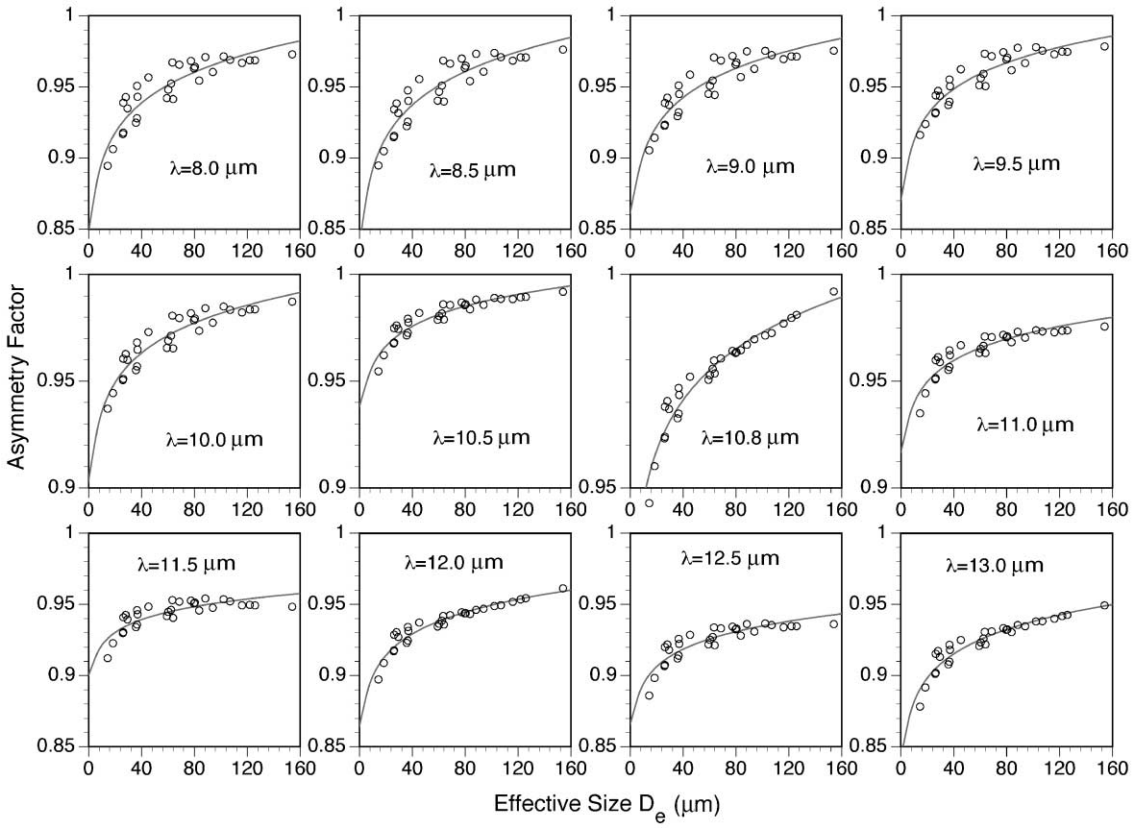

Fig. 17. The variation of the asymmetry factor versus D_e for the 12 wavelengths (circle symbols). The solid lines are the parameterization results based on power-law fitting.

Table 3
The fitting coefficients for the parameterization of the mean asymmetry parameter, which is defined by the Eq. (25)

Wavelength (μm)	ς	κ	Wavelength (μm)	ς	κ
8.0	8.317E − 1	3.279E − 2	10.8	9.092E − 1	1.771E − 2
8.5	8.217E − 1	3.565E − 2	11.0	9.080E − 1	1.501E − 2
9.0	8.399E − 1	3.120E − 2	11.5	8.922E − 1	1.394E − 2
9.5	8.560E − 1	2.779E − 2	12.0	8.519E − 1	2.355E − 2
10.0	8.917E − 1	2.092E − 2	12.5	8.553E − 1	1.932E − 2
10.5	9.271E − 1	1.387E − 2	13.0	8.290E − 1	2.682E − 2

combination of the two methods provides the results for the entire range of particle sizes over wavelengths ranging from 8 to 13 μm.

Other methods are compared but shortcomings are noted. In particular, methods based on geometric optics and anomalous diffraction theory (ADT) fail to account for the tunneling

effect (a phenomenon in which the incident energy stream outside the particle projected-area can be trapped and scattered/absorbed) in calculating the absorption and extinction efficiency. The analytical Mie theory does account for the tunneling effect. When the equivalent spherical approximation is applied to scattering by a nonspherical ice crystal, a significant overestimation of the effect can result. This is a particular problem at the size parameter where the resonance maximum is produced. For the extinction and absorption efficiency calculations, several methods including the IGOM, the Mie solution for equivalent spheres (MSFES), and ADT can lead to a substantial discontinuity at a particle size of 40 μm.

We have developed a novel new approach called the stretched scattering potential method (SSPM) to address the aforementioned difficulties. As 12 wavelengths in the spectral region 8–13 μm, we show that the SSPM is a more accurate approximation than ADT, MSFES, and IGOM. Additionally, we suggest numerical refinements to the SSPM solution. Through a combination of the FDTD and SSPM, we have computed the extinction and absorption efficiency for hexagonal ice crystals with sizes ranging from 1 to 10,000 μm at 12 wavelengths between 8 and 13 μm.

Based on the single-scattering properties obtained for individual ice crystals, 30 size distributions obtained from various field campaigns for midlatitude and tropical cirrus cloud systems have been selected to calculate the bulk scattering/absorption properties for the clouds. A parameterization effort is carried out to provide an analytical representation for these bulk scattering properties. The parameterizations are based on second-order polynomial functions for the extinction efficiency and the single-scattering albedo and a power-law form for the asymmetry parameter. We note that the volume-normalized extinction coefficient can be separated into two parts: one is inversely proportional to effective size and is independent of wavelength, and the other is the mean extinction efficiency. The present parameterization scheme is more accurate than conventional parameterization efforts because only the latter part of the volume-normalized extinction coefficient (i.e., the mean extinction efficiency) is approximated in terms of an analytical expression. Finally, we note that the single-scattering properties of ice crystals in the IR window region show a very strong wavelength dependence. This is particularly true for the single-scattering albedo. Numerical results show that the single-scattering albedo decreases with an increase in particle size for wavelengths shorter than 10.0 μm; the opposite pattern is observed for longer wavelengths. The results obtained in this study will be useful for both aircraft- and space-based IR retrieval of ice clouds.

Acknowledgements

Dr. Q. Fu is thanked for providing the data of the size distributions used in this study. The constructive comments from Dr. F. Evans are appreciated. The authors also thank the anonymous reviewer for constructive comments and suggestions. This research has been supported by a grant of NASA's MODIS project and partially by the Office of Naval Research. This study was also supported by the Atmospheric Radiation Measurement (ARM) program sponsored by the US Department of Energy (DOE) under Contract DE-A102-00ER62901 and by NASA/EOS grant (contract No. S97894-F).

References

[1] Liou KN. Influence of cirrus clouds on weather and climate processes: a global perspective. Mon Wea Rev 1986;114:1167–99.

[2] Stephens GL, Tsay SC, Stackhose PW, Flatau PJ. The relevance of the microphysical and radiative properties of cirrus clouds to climate and climate feedback. J Atmos Sci 1990;47:1742–53.

[3] Randall DA, Harshvardhan, Dazlich DA, Gorsetti TG. Interactions among radiation, convection, and large-scale dynamics in a general circulation model. J Atmos Sci 1989;46:1943–70.

[4] Starr DO. A cirrus cloud experiment: intensive field observations planned for FIRE. Bull Amer Meteor Soc 1987;68:119–24.

[5] Francis PN, Jones A, Saunders RW, Shine KP, Slingo A, Sun Z. An observational and theoretical study of the radiative properties of cirrus: some results from ICE'89. Quart J Roy Meteor Soc 1994;120:809–48.

[6] Winker DM, Couch RH, McCormick MP. An overview of LITE: NASA's Lidar in-space technology experiment. Proc IEEE 1996;84:164–80.

[7] King MD, Kaufman YJ, Menzel WP, Tanre D. Remote sensing of cloud, aerosol, and water vapor properties from the moderate resolution imaging spectrometer (MODIS). IEEE Trans Geosci Remote Sensing 1992;30:2–26.

[8] Winker DM, Wielicki BA. The PICASSO-CENA mission. Sensors, systems, and next-generation satellites III. Proc SPIE 1999;3870:26–36.

[9] Menzel WP, Wylie DP, Strabala KI. Seasonal and diurnal changes in cirrus clouds as seen in four years of observations with the VAS. J Appl Meteor 1983;22:377–84.

[10] Frey RA, Baum BA, Menzel WP, Ackerman SA, Moeller CC, Spinhirne JD. A comparison of cloud top heights computed from airborne lidar and MAS radiance data using CO_2 slicing. J Geophys Res 1999;104:24,547–55.

[11] Stubenrauch CJ, Holz R, Chedin A, Mitchell DL, Baran AJ. Retrieval of cirrus ice crystal sizes from 8.3 and 11.1 μm emissivities determined by the improved initialization inversion of TIROS-N operational vertical sounder observations. J Geophys Res 1999;104:31,793–808.

[12] Chung S, Ackerman SA, van Delst PF, Menzel WP. Model calculations and interferometer measurements of ice-cloud characteristics. J Appl Meteor 2000;39:634–44.

[13] Strabala KI, Ackerman SA, Menzel WP. Cloud properties inferred from 8–12 μm data. J Appl Meteor 1994;2:212–29.

[14] Baum BA, Soulen PF, Strabala KI, King MD, Ackerman SA, Menzel WP, Yang P. Remote sensing of cloud properties using MODIS Airborne Simulator imagery during SUCCESS. II. Cloud thermodynamic phase. J Geophys Res 2000;105:11,781–92.

[15] Revercomb HE, Buijs H, Howell HB, Laporte DD, Smith WL, Sromovsky LA. Radiometric calibration of IR Fourier transform spectrometers: solution to a problem with the high spectral resolution interferometer sounder. Appl Opt 1998;27:3210–8.

[16] Smith WL, Revercomb HE, Knuteson RO, Best FA, Dedecker R, Howell HB, Woolf M. Cirrus cloud properties derived from high spectral resolution infrared spectrometry during FIRE II. Part I: The high resolution interferometer sounder (HIS) systems. J Atmos Sci 1995;52:4238–45.

[17] Ackerman SA, Smith WL, Spinhirne JD, Revercomb HE. The 27–28 October 1986 FIRE IFO cirrus case study: Spectral properties of cirrus clouds in the 8–12 μm window. Mon Wea Rev 1990;118:2377–88.

[18] Revercomb HE, Walden VP, Tobin DC, Janderson FA, Best N, Ciganovich, Dedecker RG, Dirkx T, Ellington SC, Garcia RK, Herbsleb R, Knuteson RO, LaPorte D, McRae D, Werner M. Recent results from two new aircraft-based Fourier-transform interferometers: the scanning high-resolution interferometer sounder and the NPOESS atmospheric sounder testbed interferometer. Eighth International Workshop on Atmospheric Science from Space using Fourier Transform Spectrometry (ASSFTS), Toulouse, France, 16–18 November 1998.

[19] Takano Y, Liou KN, Minnis P. The effects of small ice crystals on cirrus infrared radiation properties. J Atmos Sci 1992;49:1487–93.

[20] Heymsfield AJ, Platt CMR. A parameterization of the particle size spectrum of ice clouds in terms of the ambient temperature and the ice water content. J Atmos Sci 1984;41:846–56.

[21] Mitchell DL, Macke A, Liu Y. Modeling cirrus clouds, II. Treatment of radiative properties. J Atmos Sci 1996;53:2967–88.

[22] Liou KN, Takano Y, Yang P. Light scattering and radiative transfer in ice crystal clouds: applications to climate research. In: Mishchenko MI, Hovenier JW, Travis LD, editors. Light scattering by nonspherical particles: theory, measurements and applications. San Diego: Academic Press, 1999.
[23] Mishchenko MI, Rossow WB, Macke A, Lacis AA. Sensitivity of cirrus cloud albedo, bidirectional reflectance and optical thickness retrieval accuracy to ice particle shape. J Geophys Res 1996;102:16,973–85.
[24] Liou KN, Takano Y. Light scattering by nonspherical particles: remote sensing and climatic implications. Atmos Res 1994;31:271–98.
[25] Minnis P, Liou KN, Takano Y. Inference of cirrus cloud properties using satellite-observed visible and infrared radiances, I. Parameterization of radiance fields. J Atmos Sci 1993;50:1279–304.
[26] Minnis P, Liou KN, Takano Y. Inference of cirrus cloud properties using satellite-observed visible and infrared radiances, II. Verification of theoretical cirrus radiative properties. J Atmos Sci 1993;50:1305–22.
[27] Han Q, Rossow WB, Chou J, Kuo KS, Welch RM. The effects of aspect ratio and surface roughness on satellite retrievals of ice-cloud properties. JQSRT 1999;63:559–83.
[28] Fu Q. An accurate parameterization of the solar radiative properties of cirrus clouds for climate models. J Climate 1996;9:2058–82.
[29] Fu Q, Yang P, Sun WB. An accurate parameterization of the infrared radiative properties of cirrus clouds for climate models. J Climate 1998;25:2223–37.
[30] Fu Q, Sun WB, Yang P. On modeling of scattering and absorption by cirrus nonspherical ice particles at thermal infrared wavelengths. J Atmos Sci 1999;56:2937–47.
[31] Wyser K, Yang P. Average crystal size and bulk shortwave single scattering properties in ice clouds. J Atmos Res 1998;49:315–35.
[32] Baum BA, Kratz D, Yang P, Ou SC, Hu YX, Soulen PF, Tsay SC. Remote sensing of cloud properties using MODIS Airborne Simulator imagery during SUCCESS. I. Data and models. J Geophys Res 2000;105: 11,767–80.
[33] Baum BA, Spinhirne J. Remote sensing of cloud properties using MODIS airborne simulator imagery during SUCCESS. III. Cloud overlap. J Geophys Res 2000;105:11,793–804.
[34] Mishchenko MI, Hovenier JW, Travis LD, editors. Light scattering by nonspherical particles: theory, measurements, and applications. San Diego: Academic Press, 1999.
[35] Yang P, Liou KN. Light scattering by hexagonal ice crystals: comparison of finite-difference time domain and geometric optics methods. J Opt Soc Amer A 1995;12:162–76.
[36] Yang P, Liou KN. Finite-difference time domain method for light scattering by small ice crystals in three-dimensional space. J Opt Soc Amer A 1996;13:2072–85.
[37] Yang P, Liou KN. An efficient algorithm for truncating spatial domain in modeling light scattering by finite-difference technique. J Comput Phys 1998;140:346–69.
[38] Yang P, Liou KN. Finite-difference time domain method for light scattering by nonspherical and inhomogeneous particles: theory, measurements, and applications. In: Mishchenko MI, Hovenier JW, Travis LD, editors. Light scattering by nonspherical particles: theory, measurements, and applications. San Diego: Academic Press, 1999.
[39] Sun WB, Fu Q, Chen Z. Finite-difference time-domain solution of light scattering by dielectric particles with a perfectly matched layer absorbing boundary condition. Appl Opt 1999;28:3141–51.
[40] Yang P, Liou KN, Mishchenko MI, Gao BC. Efficient finite-difference time-domain scheme for light scattering by dielectric particles: applications to aerosols. Appl Opt 2000;39:3727–37.
[41] Yang P, Liou KN. Geometric-optics-integral-equation method for light scattering by nonspherical ice crystals. Appl Opt 1996;35:6568–84.
[42] Yang P, Liou KN. Light scattering by hexagonal ice crystals: solution by ray-by-ray integration algorithm. J Opt Soc Amer A 1997;14:2278–89.
[43] Nussenzveig HM. Diffraction effects in semiclassical scattering. New York: Cambridge University Press, 1992.
[44] Mitchell DL. Parameterization of the Mie extinction and absorption coefficients for water clouds. J Atmos Sci 2000;57:1311–26.
[45] Baran AJ, Havemann S. Rapid computation of the optical properties of hexagonal columns using complex angular momentum theory. JQSRT 1999;63:499–519.
[46] Nussenzveig HM, Wiscombe WJ. Efficiency factors in Mie scattering. Phys Rev Lett 1980;45:1490–4.

[47] Nussenzveig HM, Wiscombe WJ. Diffraction as tunneling. Phys Rev Lett 1987;59:1667–70.
[48] Baran AJ, Foot JS, Mitchell DL. The question of ice crystal absorption: a comparison between T-matrix, Mie, and anomalous diffraction theory and implications for remote sensing. Appl Opt 1998;37:2207–15.
[49] Korolov AV, Issac GA, Hallett J. Ice particle habits in artic clouds. Geophys Res Lett 1999;26:1299–302.
[50] Heymsfield AJ, Iaquinta J. Cirrus crystal terminal velocities. J Atmos Sci 2000;57:916–38.
[51] Takano Y, Liou KN. Radiative transfer in cirrus clouds. I. Single-scattering and optical properties of hexagonal ice crystals. J Atmos Sci 1989;46:3–19.
[52] Takano Y, Liou KN. Radiative transfer in cirrus clouds. II. Theory and computation of multiple scattering in an anisotropic medium. J Atmos Sci 1989;46:20–36.
[53] Ebert EE, Curry JA. A parameterization of ice cloud optical properties for climate models. J Geophys Res 1992;97:3831–6.
[54] Ono A. The shape and riming properties of ice crystals in natural clouds. J Atmos Sci 1969;26:138–47.
[55] Auer Jr AH, Veal DL. The dimension of ice crystals in natural clouds. J Atmos Sci 1970;27:919–26.
[56] Warren S. Optical constants of ice from the ultraviolet to the microwave. Appl Opt 1984;23:1206–25.
[57] Carlon HR. Christiansen effect in IR spectra of soil-derived atmospheric dusts. Appl Opt 1976;18:3610–4.
[58] Arnott WP, Dong YY, Hallett J. Extinction efficiency in the infrared (2–18 μm) of laboratory ice clouds: observations of scattering minima in the Christiansen bands of ice. Appl Opt 1995;34:541–51.
[59] Schmitt CG, Arnott WP. Infrared emission (500–2000 cm^{-1}) of laboratory ice clouds. JQSRT 2000;63:701–25.
[60] Yang P, Liou KN, Arnott WP. 1997: Extinction efficiency and single-scattering albedo of ice crystals in laboratory and natural cirrus clouds. J Geophys Res 1997;102:21,825–35.
[61] Wiscombe WJ. The delta-M method: rapid yet accurate radiative flux calculations for strongly asymmetric phase functions. J Atmos Sci 1977;34:1408–22.
[62] Stratton JA. Electromagnetic theory. New York: McGraw-Hill, 1941.
[63] Yang P, Gao BC, Baum BA, Hu YX, Wiscombe WJ, Mishchenko MI, Winker DM, Nasiri SL. Asymptotic solutions for optical properties of large particles with strong absorption. Appl Opt 2001;40:1532–47.
[64] Mitchell DL, Arnott WP. A model predicting the evolution of ice particle size spectra and radiative properties of cirrus clouds. Part II: Dependence of absorption and extinction on ice crystal morphology. J Atmos Sci 1994;51:817–32.
[65] Yang P, Liou KN, Wyser K, Mitchell D. Parameterization of the scattering and absorption properties of individual ice crystals. J Geophys Res 2000;105:4699–718.
[66] Grenfell TC, Warren SG. Representation of a nonspherical ice particle by a collection of independent spheres for scattering and absorption of radiation. J Geophys Res 1999;104:31,697–709.
[67] Mugnai A, Wiscombe WJ. Scattering from nonspherical Chebyshev particles. 1. Cross sections, single-scattering albedo, asymmetry factor, and backscattered fraction. Appl Opt 1986;25:1235–44.
[68] Mishchenko MI. Light scattering by size-shape distributions of randomly oriented axially symmetric particles of a size comparable to a wavelength. Appl Opt 1993;32:4652–66.
[69] Purcell EM, Pennypacker CR. Scattering and absorption of light by nonspherical dielectric grains. Astrophys J 1973;186:705–14.
[70] Draine BT, Flatau PJ. Discrete-dipole approximation for scattering calculations. J Opt Soc Am A 1994;11:1491–9.
[71] van de Hulst HC. Light scattering by small particles. New York: Wiley, 1957.
[72] Chylek P, Klett JD. Extinction cross sections of nonspherical particles in the anomalous diffraction approximation. J Opt Soc Am A 1991;8:274–81.
[73] Liu Y, Arnott WP, Hallett J. Anomalous diffraction theory for arbitrarily oriented finite circular cylinders and comparison with exact T-matrix results. Appl Opt 1998;37:5019–30.
[74] Sun WB, Fu Q. Anomalous diffraction theory for arbitrarily oriented hexagonal crystals. JQSRT 1999;63: 727–37.
[75] Schiff LI. Approximation method for short wavelength or high-energy scattering. Phys Rev 1956;104:1481–5.
[76] Glauber RJ. High-energy collision theory. In: Britten WE, Dunham LC, editors. Lectures in theoretical physics. New York: Interscience, 1959.
[77] Chen TW. High energy light scattering in the generalized eikonal approximation. Appl Opt 1989;28:4096–102.

[78] Perrin JM, Chiappeta P. Light scattering by large particles I. A new theoretical description in the eikonal picture. Opt Acta 1985;32:907–21.
[79] Wiscombe WJ. Improved Mie scattering algorithms. Appl Opt 1980;19:1505–9.
[80] Mitchell DL, Chai SK, Liu Y, Heymsfield AJ, Dong Y. Modeling cirrus clouds. Part I: treatment of bimodal size spectra and case study analysis. J Atmos Sci 1996;53:2952–66.
[81] McFarquhar GM, Heymsfield AJ. Microphysical characteristics of three cirrus anvils sampled during the central equatorial pacific experiment. J Atmos Sci 1996;53:2401–23.
[82] McFarquhar GM, Heymsfield AJ, Macke A, laquinta J, Aulenbach SM. Use of observed ice crystal sizes and shapes to calculate mean scattering properties and multi-spectral radiances: CEPEX 4 April 1993 case study. J Geophys Res 1999;104:31,763–79.
[83] Foot JS. Some observations of the optical properties of clouds. Part II: Cirrus. Quart J Roy Meteor Soc 1988;114:145–64.
[84] Hansen JE, Travis LD. Light scattering in planetary atmosphere. Space Sci Rev 1974;16:527–610.
[85] Liou KN, Yang P, Takano Y, Sassen K, Charlock T, Arnott W. On the radiative properties of contrail cirrus. Geophys Res Lett 1998;25:1161–4.